remote sensing

MDPI

Article

Harnessing Satellite Data to Evaluate Global Biodiversity Hypotheses Across Seasonal and Inter-Annual Scales

Kedi Liu [1,2], Yi Li [1,2], Kaiyue Luo [1,2], Chunyan Cao [1,2] and Xuanlong Ma [1,2,*]

[1] MoE Key Laboratory of Western China's Environmental Systems, College of Earth and Environmental Sciences, Lanzhou University, No. 222 South Tianshui Road, Lanzhou 730000, China; 220220948050@lzu.edu.cn (K.L.); yili2025@lzu.edu.cn (Y.L.); luoky2024@lzu.edu.cn (K.L.); caochy2023@lzu.edu.cn (C.C.)

[2] Center for Remote Sensing of Ecological Environments in Cold and Arid Regions, Lanzhou University, No. 222 South Tianshui Road, Lanzhou 730000, China

* Correspondence: xlma@lzu.edu.cn

Highlights

What are the main findings?

- We extend the Dynamic Habitat Index (DHI) framework by integrating both seasonal and inter-annual productivity dynamics into a unified six-dimensional system.
- The enhanced DHI significantly improves global species richness prediction performance (cross-validated $R^2 = 0.89$) using a random forest model.

What are the implications of the main findings?

- Inter-annual productivity variability emerges as the most influential predictor, highlighting the dominant role of environmental stability in shaping biodiversity patterns.
- The extended framework provides a scalable tool linking satellite remote sensing with macroecological patterns, supporting biodiversity conservation under global environmental change.

Abstract

Monitoring species richness patterns across large spatial scales is essential for addressing the global biodiversity crisis. Dynamic Habitat Indices (DHIs), derived from satellite-based productivity data, have proven valuable for predicting species distributions. The original DHI framework comprises three complementary sub-indices, each corresponding to a key ecological hypothesis linking productivity and biodiversity: annual cumulative productivity (DHI Cum; *available energy* hypothesis), annual minimum productivity (DHI Min; *environmental stress* hypothesis), and the coefficient of variation in productivity (DHI CV; *environmental stability* hypothesis). However, current DHI formulations primarily focus on intra-annual vegetation productivity dynamics, thereby overlooking the ecological significance of inter-annual productivity variability. To address this limitation, we propose an extended DHI suite that integrates both seasonal (intra-annual) and long-term (inter-annual) productivity metrics. Using a random forest regression approach, we demonstrate that incorporating this extended DHI suite significantly improves predictions of global vertebrate species richness (cross-validated $R^2 = 0.89$, RMSE = 68.20) compared to using seasonal metrics alone ($R^2 = 0.86$). Notably, inter-annual productivity variation emerged as the most influential predictor, strongly supporting the *environmental stability* hypothesis. This was followed by importance in seasonal minimum productivity (*environmental stress*) and cumulative productivity (*available energy*). Our findings reveal the critical, complementary roles of seasonal and inter-annual productivity dynamics in shaping global faunal species richness patterns. This enhanced framework provides a robust

Check for updates

Academic Editor: Mohammadmehdi Saberioon

Received: 9 May 2026
Revised: 12 June 2026
Accepted: 15 June 2026
Published: 25 June 2026

Copyright: © 2026 by the authors. Licensee MDPI, Basel, Switzerland. This article is an open access article distributed under the terms and conditions of the Creative Commons Attribution (CC BY) license.

scalable tool for assessing species richness distributions and informing conservation strategies amid accelerating climate shifts and anthropogenic pressures.

Keywords: terrestrial ecology; biodiversity monitoring; conservation; habitat quality; global change

1. Introduction

The world is experiencing an unprecedented decline in biodiversity, driven primarily by habitat destruction, invasive species, and the escalating impacts of climate change—a convergence of threats now widely recognized as the global biodiversity crisis [1,2]. This rapid decline threatens vital ecosystem functions and Nature's Contributions to People (NCP), undermining critical services such as carbon sequestration, soil and water conservation, and the sustainable provisioning of food and timber resources [3,4]. In response, major international bodies, including IPBES (Intergovernmental Science-Policy Platform on Biodiversity and Ecosystem Services) and the UN CBD (United Nations Convention on Biological Diversity), are mobilizing collaborative efforts with national governments and scientific agencies to implement immediate actions to curb further biodiversity loss.

Mitigating this crisis requires comprehensive monitoring of species richness and habitat quality across broad spatial and temporal scales. However, accurately mapping global biodiversity patterns remains a formidable challenge, constrained by pervasive spatial data gaps and the inherent complexity of ecological systems [5,6]. These limitations continue to hinder effective conservation planning, despite the consensus that robust assessments of habitat conditions and species distributions are fundamental for predicting ecological responses to environmental change [5,7]. While biodiversity conservation is inherently multidimensional, maintaining habitat quality and preserving species richness are paramount objectives; notably, species richness is enshrined as a core component within the GEO BON (Group on Earth Observation Biodiversity Observation Network) EBVs (Essential Biodiversity Variables) framework for global monitoring [4].

Conventional field-based surveys, while foundational, are labor-intensive, cost-prohibitive, and spatially restricted. Consequently, they cannot provide the consistent, broad-scale, and long-term continuous assessments required for global biodiversity monitoring [8]. Satellite remote sensing offers a transformative solution by continuously capturing critical land surface dynamics that covary with species distribution patterns, effectively overcoming the spatiotemporal limitations of traditional surveys [9–11]. Current remote sensing methodologies for monitoring species richness broadly follow two pathways: (1) establishing direct empirical correlations between spectral characteristics (e.g., surface reflectance, radar backscatter, or simple vegetation indices) and field-observed species data [12–14]; and (2) deriving integrative, theoretically grounded indices that encapsulate key ecological hypotheses governing species richness patterns. Within the latter pathway, Dynamic Habitat Indices (DHIs) have emerged as exceptionally valuable tools. By transforming time-series vegetation productivity data into actionable, biologically meaningful metrics, DHIs bridge the gap between ecosystem functioning and regional-to-global biodiversity assessments [15–19].

The theoretical framework of Dynamic Habitat Indices (DHIs) is built upon three fundamental ecological hypotheses linking vegetation productivity to species richness patterns: (1) the *available energy* hypothesis [20,21], which asserts that greater annual productivity enhances species richness by increasing overall energy availability; (2) the *environmental stress* hypothesis [22,23], which posits that elevated minimum productivity mitigates environmental stress, thereby supporting higher biodiversity; and (3) the *environmental stability* hypothesis [24], which suggests that reduced variability in productivity promotes species richness by ensuring a stable

resource supply. These theoretical foundations have been traditionally operationalized through three corresponding seasonal DHI metrics: Cum_s (cumulative annual productivity reflecting total energy), Min_s (minimum annual productivity indicating stress tolerance thresholds), and CV_s (the coefficient of variation in productivity measuring environmental stability) [15]. The subscript 's' denotes that these indices are derived from seasonal, or intra-annual, productivity profiles—a methodological standard we detail in the following sections.

Although these seasonal DHIs have proven highly valuable in conservation biology, relying exclusively on intra-annual productivity profiles derived from a single growing season presents a critical limitation. While intra-annual variations successfully capture baseline phenological cycles, they inherently obscure the ecological significance of inter-annual productivity dynamics. Long-term climatic trends, multi-year extreme events (e.g., ENSO cycles), and gradual environmental shifts fundamentally govern species survival and reproductive success over time [25–27]. Crucially, local extinctions are frequently driven by episodic, resource-limited periods, even if average intra-annual conditions appear stable [28] or overall climatic suitability is improving [29]. A comprehensive meta-analysis of 519 studies by [30] emphasizes that extreme weather events disproportionately stress populations—a mechanism highly pertinent to the DHI frameworks of environmental stress and stability. Furthermore, climate-induced resource bottlenecks [31] act as severe ecological filters, demonstrating how inter-annual variability robustly structures biodiversity. Supporting this, a recent study evaluating annual variations in DHIs across the United States has demonstrated that explicitly accounting for year-to-year productivity dynamics can explain up to 75% of the temporal variance in bird species richness [32].

Current DHI formulations, which smooth out these critical inter-annual fluctuations by focusing on mean annual conditions, may therefore systematically underestimate habitat vulnerability. For instance, drought-induced productivity crashes can drastically reduce species richness [33]; capturing these events requires expanding the DHI framework to integrate inter-annual productivity variations. Doing so not only addresses current methodological gaps but also provides a more ecologically comprehensive representation of the three foundational hypotheses. We therefore hypothesize that: (1) long-term maximum productivity will complement seasonal cumulative productivity in capturing absolute *available energy* capacity; (2) inter-annual variability will critically enrich the *environmental stability* hypothesis beyond mere seasonal fluctuations; and (3) decadal minimum productivity will explicitly enhance the *environmental stress* hypothesis by capturing the severe impacts of extreme low-productivity events. Validating these hypotheses would align the DHI framework more closely with real-world ecosystem functioning, where species distributions are jointly constrained by both seasonal rhythms and inter-annual volatility.

To bridge this gap, this study tests the overarching hypothesis that incorporating inter-annual productivity dynamics into conventional DHIs will significantly improve the prediction of global faunal species richness patterns. We pursue three specific objectives: (1) to develop a novel suite of long-term DHI metrics derived from multi-year satellite vegetation productivity records; (2) to examine the global-scale spatial relationships between these long-term indices and species richness patterns; and (3) to quantitatively assess their additive explanatory power relative to traditional seasonal DHIs. To operationalize this, we integrated both seasonal and long-term productivity metrics into a robust Random Forest predictive framework.

2. Materials and Methods

2.1. Satellite Gross Primary Productivity (GPP) Dataset

To calculate both seasonal and long-term DHIs at the global scale, we utilized the eLUE-derived Gross Primary Productivity (GPP) dataset (GPP_{eLUE}), which spans from 2001 to 2024 [34]. This dataset was generated using the ecosystem Light Use Efficiency (eLUE)

model framework, which integrates MODIS Enhanced Vegetation Index (EVI) data and is robustly calibrated against in situ GPP measurements from 120 FLUXNET2015 tower sites [34–36]. Rigorous validation across these 120 sites (comprising 953 site-years) demonstrated strong model performance (cross-validated $R^2 = 0.74$, RMSE = 2.05 g C m^{-2} d^{-1}) [36]. The GPP_{eLUE} product features a spatial resolution of 0.05° and a monthly temporal resolution. It is publicly accessible via the Dryad Digital Repository (https://doi.org/10.5061/dryad.v9s4mw74h, accessed on 14 June 2026) [34].

The systematic error characteristics and inter-product consistency of the GPP_{eLUE} dataset have been thoroughly evaluated in a recent study by [36]. Benchmarked against 120 global FLUXNET sites, the GPP_{eLUE} product demonstrated robust performance across 11 distinct biomes, capturing seasonal and inter-annual productivity dynamics with minimal bias. Notably, the dataset outperforms or performs comparably to other mainstream LUE-based and machine-learning-based global GPP products (e.g., MOD17A2H and FLUXCOM-X), thereby ensuring high reliability for deriving the macroecological Dynamic Habitat Indices utilized in this framework.

2.2. Eddy-Covariance Flux Tower Data

To validate the satellite-derived DHIs, we followed the methodological framework established by [16]. This involved utilizing in situ DHIs computed directly from eddy-covariance GPP measurements within the FLUXNET2015 database (https://fluxnet.org/data/fluxnet2015-dataset/, accessed on 14 June 2026). Half-hourly flux measurements were aggregated into daily GPP estimates (GPP_{EC}) following stringent quality control protocols. Initially, we applied the dataset's built-in quality flags. Subsequently, we implemented an additional layer of data screening adapted from [37], requiring: (1) ≤20% gap-filled data; (2) uncertainty in Net Ecosystem Exchange (NEE) measurements of <2 g C m^{-2} d^{-1}; and (3) a discrepancy of <2 g C m^{-2} d^{-1} between the daytime (GPP_DT_VUT_REF; [38] and nighttime (GPP_NT_VUT_REF; [39]) flux partitioning methods.

Following this screening, our final analysis incorporated data from 43 FLUXNET tower sites, each possessing more than three years of continuous, high-quality measurements with minimal data gaps (Figure 1; Table S1). These sites broadly represent 10 distinct plant functional types (PFTs): croplands (CRO, 9 sites), deciduous broadleaf forests (DBF, 8 sites), evergreen broadleaf forests (EBF, 4 sites), evergreen needleleaf forests (ENF, 9 sites), mixed forests (MF, 3 sites), grasslands (GRA, 5 sites), open shrublands (OSH, 1 site), closed shrublands (CSH, 1 site), savannas (SAV, 1 site), and woody savannas (WSA, 2 sites).

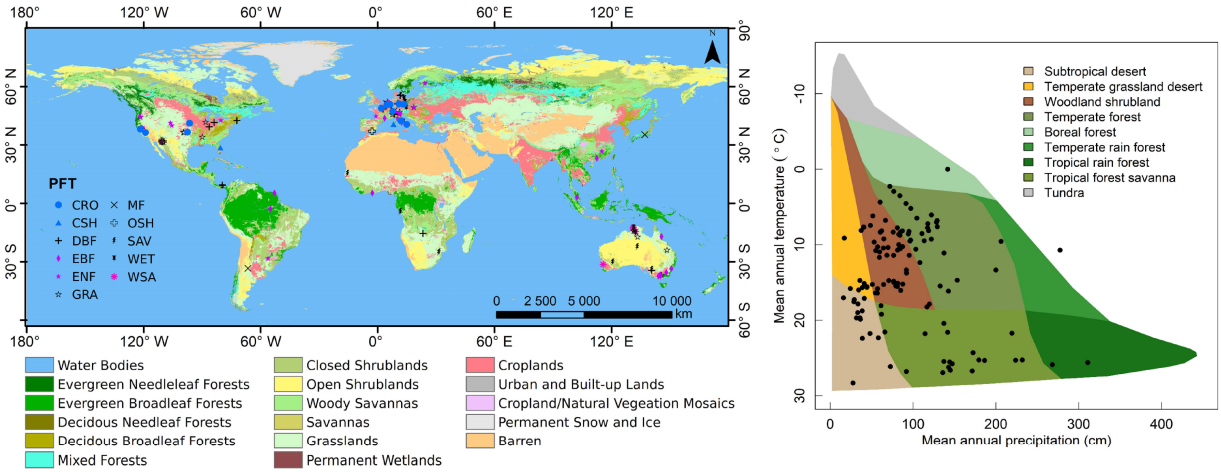


Figure 1. Geographic locations, land cover types, and the distribution of the 43 FLUXNET sites in Whittaker's bioclimatic zones. The land cover types are from MCD12C1 (v061) global MODIS/Terra + Aqua Land Cover Type Yearly L3 Global 0.05Deg CMG product [40].

2.3. IUCN Red List Species Richness Data

To evaluate the relationships between satellite-derived DHIs and global biodiversity patterns, we utilized species richness data from the International Union for Conservation of Nature (IUCN) (https://www.iucnredlist.org/resources/other-spatial-downloads, accessed on 14 June 2026). This comprehensive dataset integrates distribution records for four major terrestrial vertebrate classes: amphibians [41], birds, mammals, and reptiles [42], provided at a 30 km × 30 km grid resolution. The range maps encompass all species with known distributions, irrespective of their current IUCN conservation status. Notably, these range maps were generated through the spatial interpolation of occurrence records contributed by researchers worldwide, rather than relying on predictive climatic modeling. While these data represent the most complete spatial information currently available for terrestrial vertebrates, we acknowledge certain limitations: (1) taxonomic coverage is primarily restricted to well-documented vertebrate groups, and (2) marine ecosystems are inherently underrepresented in this dataset.

To address spatial autocorrelation—where neighboring grids often lack independence within DHI or species richness strata [17]—we aggregated 30 km grids into 210 km grids using a mean aggregation method following [16]. After excluding regions with missing data, we analyzed 1806 aggregated grids globally, ensuring a minimum of 100 grids per each of the 6 biogeographic realm (ranging from 125 to 747).

2.4. Biogeographic Realm

We used biogeographic realm classification to evaluate the performance of DHI-based models across distinct global ecological regions (Figure 2). Our analysis encompassed six major realms: Australia (AA), Afrotropic (AT), Indo-Malay (IM), Nearctic (NA), Neotropic (NT), and Palearctic (PA). The Antarctic and Oceanian realms were excluded due to spatial data limitations. Realm boundaries were delineated using the WWF Terrestrial Ecoregions dataset ([43]; https://www.worldwildlife.org/biomes, accessed on 14 June 2026), facilitating a robust regional assessment of model predictability across contrasting biogeographic contexts.

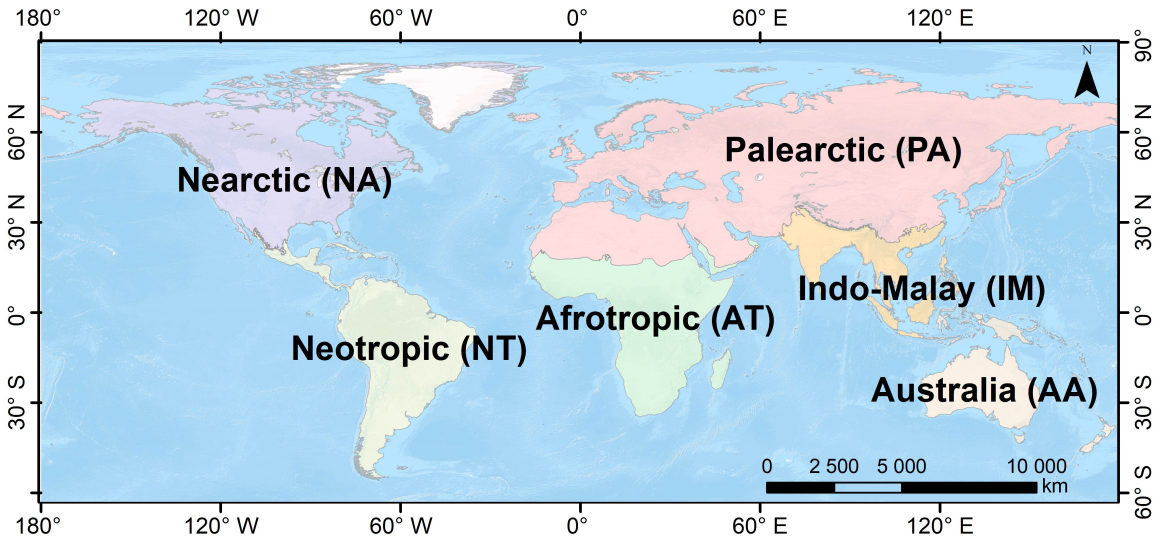


Figure 2. Spatial distribution of the six biogeographic realms evaluated in this study. PA: Palearctic; IM: Indo-Malay; AA: Australia; AT: Afrotropic; NA: Nearctic; NT: Neotropic. Realm boundaries were derived from the WWF Terrestrial Ecoregions dataset (https://www.worldwildlife.org/biomes, accessed on 14 June 2026).

2.5. Calculation of the Seasonal DHIs Metrics

We derived three seasonal DHI metrics from both the satellite-derived (GPP_{eLUE}) and in situ (GPP_{EC}) productivity datasets: (1) Cumulative Annual Productivity (Cum_s), representing total annual photosynthetic activity; (2) Minimum Annual Productivity (Min_s), indicating critical resource availability during limiting periods; and (3) Intra-annual Variability (CV_s), quantifying seasonal fluctuations in productivity. These indices were calculated as follows:

$$\mathrm{Cum_s} = \sum_{t=1}^{n} p_t \tag{1}$$

$$\mathrm{Min_s} = \min(p_t) \tag{2}$$

$$\mathrm{CV_s} = \frac{\sigma_t}{\mu_t} \tag{3}$$

where p_t denotes the monthly GPP value from either source, and t represents the monthly timestep (1–12). To mitigate the influence of short-term temporal anomalies on the seasonal DHI metrics, we derived a mean decadal phenology curve for each pixel by averaging the productivity across all ten years for each corresponding month. This composite phenology curve, termed the mean seasonal profile, was subsequently utilized to calculate the three seasonal DHIs. Utilizing this composited approach ensures robust baseline intra-annual profiles and enables direct, standardized comparisons with the long-term DHIs evaluated over the same decadal period.

2.6. Calculation of the Long-Term DHIs

To capture inter-annual productivity dynamics, we extended the traditional DHI framework by developing three decadal-scale metrics: (1) Maximum Annual Productivity (Max_{lt}), representing peak decadal carrying capacity; (2) Minimum Annual Productivity (Min_{lt}), indicating absolute stress tolerance thresholds over the long term; and (3) Inter-annual Variability (CV_{lt}), reflecting broader ecosystem stability (Figure 3). These long-term indices were calculated as follows:

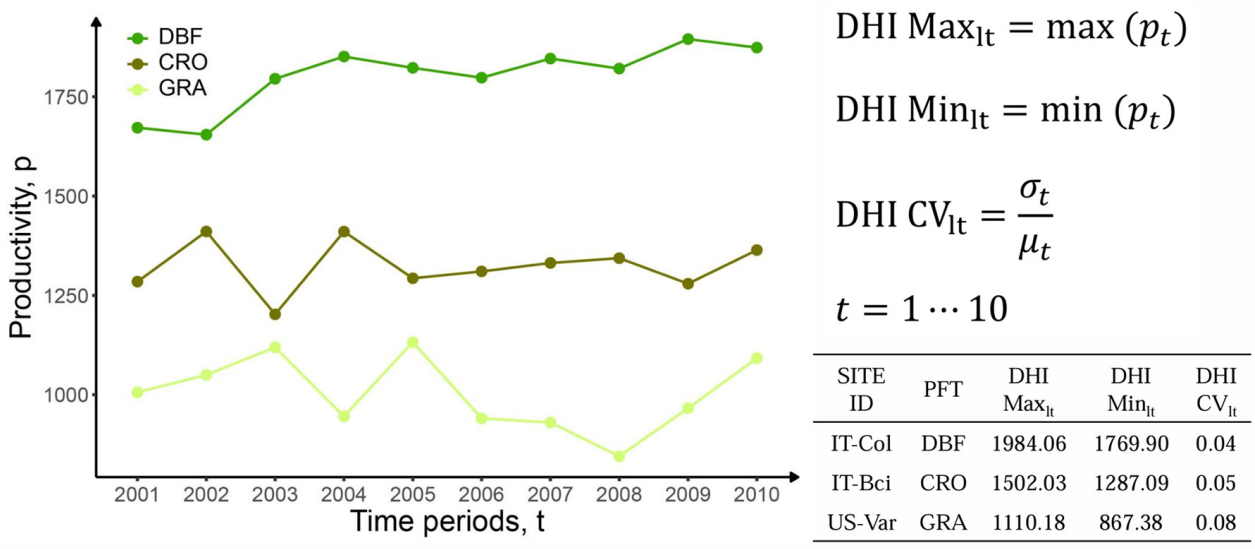
$$\mathrm{Max_{lt}} = \max(p_t) \tag{4}$$

$$\mathrm{Min_{lt}} = \min(p_t) \tag{5}$$

$$\mathrm{CV_{lt}} = \frac{\sigma_t}{\mu_t} \tag{6}$$

where p_t represents the annual total GPP (summed from monthly data for each year) derived from either GPP_{eLUE} or GPP_{EC}, and t corresponds to the specific year within the 10-year decadal period ($t = 1 \ldots 10$). By computing the annual GPP time series for each pixel, we effectively captured critical year-to-year fluctuations. Figure 3 illustrates the conceptual definitions of these long-term DHIs alongside representative GPP time series for distinct biomes (forest, cropland, and grassland).

To derive robust long-term productivity indicators (Max_{lt}, Min_{lt}, and CV_{lt}), we implemented a rolling-window approach covering the entire study period (2001–2024). Specifically, we calculated the DHIs for each consecutive 10-year window (e.g., 2001–2010, 2002–2011, …, 2015–2024). The final indices used for subsequent modeling were defined as the arithmetic mean of the values derived from all overlapping windows. This procedure minimizes the impact of inter-annual climatic volatility and ensures that our metrics accurately reflect the persistent environmental constraints and carrying capacity of the ecosystem, rather than transient short-term productivity fluctuations.



SITE ID	PFT	DHI Max_{lt}	DHI Min_{lt}	DHI CV_{lt}
IT-Col	DBF	1984.06	1769.90	0.04
IT-Bci	CRO	1502.03	1287.09	0.05
US-Var	GRA	1110.18	867.38	0.08

Figure 3. Conceptual calculation of the three long-term DHIs utilizing the annual total productivity (p_y) time series. The decadal maximum DHI (Max_{lt}) extracts the peak productivity value within the 10-year period; the decadal minimum DHI (Min_{lt}) identifies the lowest productivity value; and the decadal coefficient of variation DHI (CV_{lt}) quantifies inter-annual variability using the standard deviation (σ) and the mean (μ) across all years.

It is theoretically important to note that the long-term DHIs and the traditional seasonal DHIs are intentionally calculated in distinct mathematical spaces to achieve ecological information complementarity. The seasonal DHIs are derived from the decadal average of monthly mean GPP, a smoothing process necessary to isolate the predictable, climatological baseline of intra-annual phenology by filtering out inter-annual noise. Conversely, the long-term DHIs are computed directly from the un-smoothed decadal time series of annual total GPP. This un-smoothed mathematical space is strictly required to preserve and extract the genuine inter-annual volatility and resource extremes (e.g., decadal peak carrying capacity and minimum stress thresholds) that would otherwise be masked by multi-year averaging. By decoupling these mathematical spaces, our extended framework effectively separates the stable habitat baseline from unpredictable environmental boundaries without confounding the two signals.

2.7. Principal Component Analysis (PCA)

We applied principal component analysis (PCA) to the six DHI metrics (Cum_{s}, Min_{s}, CV_{s}, Max_{lt}, Min_{lt}, CV_{lt}) to evaluate their multivariate structure and isolate information redundancy. Prior to PCA, all indices were standardized using z-score normalization ($\mu = 0, \sigma = 1$). The PCA was implemented in R (v4.3.1) via the stats package [44], utilizing 10,000 globally distributed, randomly sampled pixels to assess the relative orthogonal contribution of each metric and guide subsequent modeling.

2.8. Random Forest Regression Prediction Model and Cross-Validation

To effectively capture the nonlinear relationships between the six DHI metrics and species richness, we constructed a Random Forest (RF) regression model. The RF algorithm generates an ensemble of decision trees utilizing bootstrap sampling, aggregating their predictions to minimize overfitting and enhance generalizability [45]. At each node split, a random subset of standardized predictors is evaluated to maintain model diversity. Model hyperparameters (specifically ntree and mtry) were optimized using the random Forest package in R (v4.3.1).

The relative contribution of each variable was quantified via permutation importance, defined as the percentage increase in the out-of-bag mean squared error (%IncMSE) when a given predictor's values are randomly permuted:

$$\%\text{IncMSE} = \frac{\text{MSE}_{\text{perm}} - \text{MSE}_{\text{orig}}}{\text{MSE}_{\text{orig}}} \quad (7)$$

Higher %IncMSE values signify a greater contribution of the predictor to the model's overall accuracy.

Model predictive performance was rigorously evaluated through 10-fold cross-validation utilizing three standard statistical metrics: the coefficient of determination (R^2), root mean squared error (RMSE), and mean absolute error (MAE), mathematically expressed as:

$$R^2 = 1 - \frac{\sum_{i=1}^{n}(y_i - \hat{y}_i)^2}{\sum_{i=1}^{n}(y_i - \overline{y})^2} \quad (8)$$

where y_i is the observed species richness, $\hat{y}_i$ is the model-predicted value, $\overline{y}$ is the mean of the observed values, and n is the total sample size. Lower RMSE and MAE values, coupled with higher R^2 values, indicate superior prediction accuracy.

To address potential concerns regarding multicollinearity among predictors (e.g., the high spatial correlation between Cum_s and Max_{lt}), we conducted a robustness check using Recursive Feature Elimination (RFE) and LASSO regression. These methods employ penalty mechanisms to identify the most stable predictors, ensuring that the variable importance rankings are not biased by shared variance. The results are detailed in Supplementary Table S3.

This RF framework enabled robust, spatially explicit predictions of global species richness while providing quantitative insights into the relative explanatory power of seasonal versus long-term productivity dynamics. All data preprocessing, statistical modeling, and spatial visualization were executed within the R statistical computing environment (version 4.3.1) [46].

3. Results

3.1. Validation of Six DHIs Metrics Using FLUXNET and Global Biogeographic Patterns

To establish confidence in the satellite-derived (GPP_{eLUE}) seasonal and long-term DHI metrics prior to their global-scale application, we first validated their accuracy against in situ measurements across the 43 selected FLUXNET sites. Strong positive correlations were observed across all metrics, yielding Pearson's R values of 0.76 (Cum_s), 0.91 (Min_s), 0.77 (CV_s), 0.76 (Max_{lt}), 0.68 (Min_{lt}), and 0.69 (CV_{lt}) (Figure 4). Five of the six indices demonstrated close adherence to the 1:1 agreement line (Figure 4a–e). However, the satellite-derived CV_{lt} systematically underestimated inter-annual variability relative to the eddy-covariance tower measurements (Figure 4f).

Figure 5 reveals the global biogeographic patterns of the six satellite-derived DHI metrics, highlighting how each metric and its corresponding productivity-species richness hypothesis vary across biomes and climatic regions. The cumulative productivity indices (Cum_s and Max_{lt}) show remarkably similar spatial distributions, both exhibiting peak values in tropical regions—consistent with high productivity expectations—while maintaining substantial values in the temperate and boreal forests of Eurasia (Figure 5a,b). In contrast, the minimum productivity indices (Min_s and Min_{lt}) demonstrate maxima in the tropics but diverge significantly in their latitudinal gradients. Specifically, Min_s displays a sharper decline with increasing latitude compared to Min_{lt}, which maintains relatively high values extending into temperate regions (Figure 5c,d). Most notably, the variability indices

exhibit opposing spatial patterns: CV_s peaks in temperate zones while showing minimal values in the tropics, reflecting strong seasonal cycles. Conversely, CV_{lt} reaches maximum values in dryland regions and minimums in humid or cold areas, effectively capturing distinct patterns of inter-annual variability (Figure 5e,f). These global patterns collectively demonstrate how the comprehensive DHI suite captures complementary dimensions of vegetation dynamics across diverse biomes and climatic regimes.

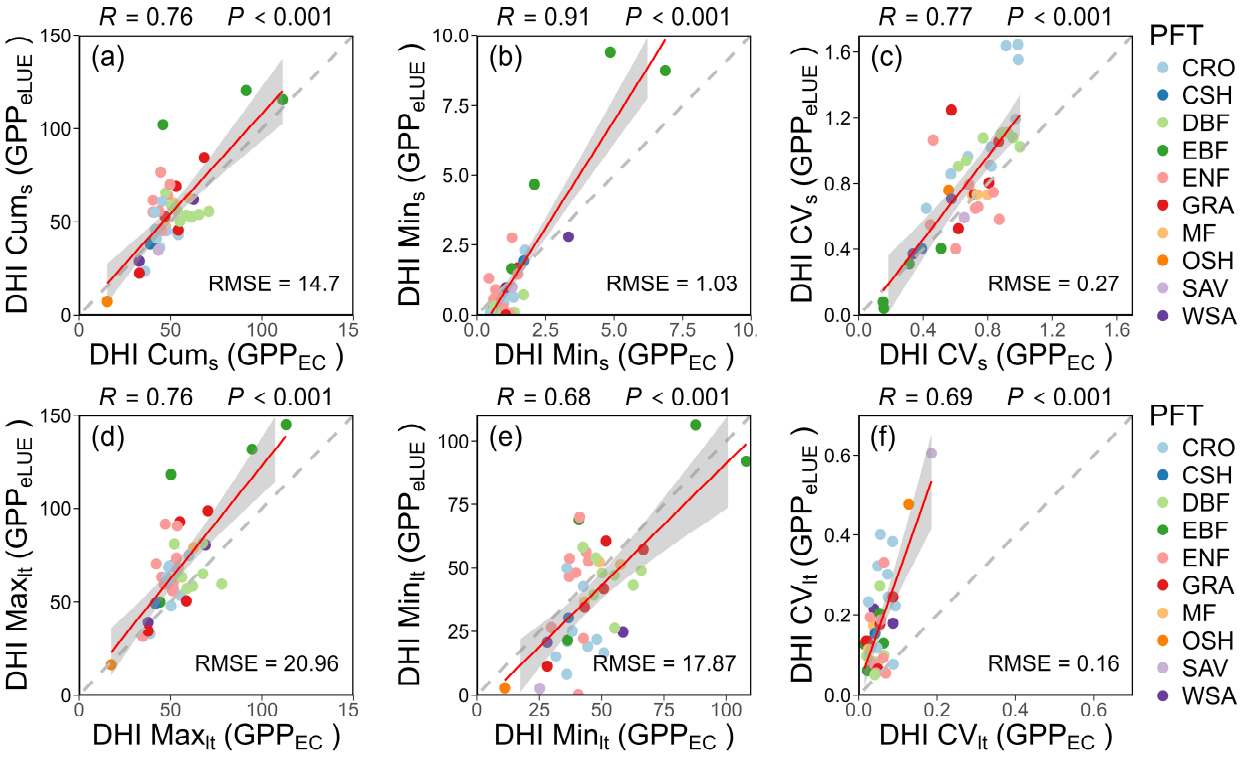


Figure 4. Scatterplots comparing the six DHIs derived from satellite GPP_{eLUE} against those derived from in situ eddy-covariance flux tower GPP across 43 FLUXNET sites. (**a**) Cum_s; (**b**) Min_s; (**c**) CV_s; (**d**) Max_{lt}; (**e**) Min_{lt}; (**f**) CV_{lt}. Pearson's correlation coefficient (R), p-value, and root mean squared error (RMSE) are labeled on each subplot for reference.

3.2. Dimensionality Analysis of the Six DHIs Metrics

The six satellite-derived DHI metrics exhibited significant intercorrelations, revealing substantial information redundancy within the dataset (Figure 6). Productivity-related indices showed particularly strong positive associations, with Pearson correlation coefficients reaching $R = 0.95$ between Cum_s and Max_{lt}, $R = 0.94$ between Max_{lt} and Min_{lt}, and $R = 0.87$ between Cum_s and Min_{lt} (all $p < 0.001$). Pairs of corresponding seasonal and long-term indices demonstrated consistently high correlations (e.g., $R = 0.95$ for Cum_s vs. Max_{lt} and $R = 0.65$ for Min_s vs. Min_{lt}, both $p < 0.001$). A notable exception occurred with the variability indices, which exhibited a significant negative correlation ($R = -0.33$, $p < 0.001$) between CV_s and CV_{lt}. These correlation patterns suggest that while most productivity-driven DHI metrics capture overlapping aspects of vegetation dynamics, the seasonal and inter-annual variability indices represent fundamentally distinct ecological dimensions of plant behavior.

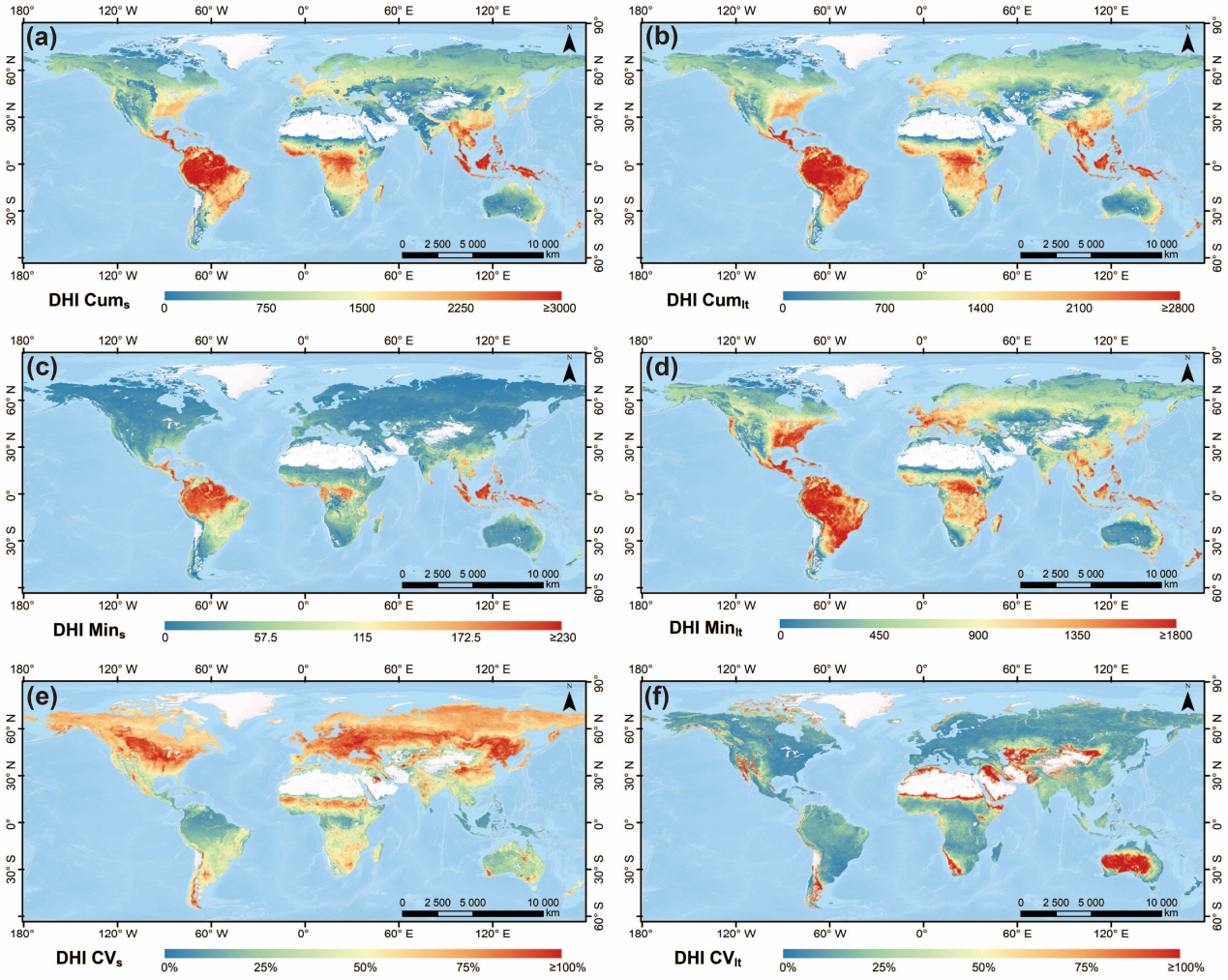


Figure 5. Spatial patterns of the seasonal and long-term satellite DHI metrics. Maps display the (**a**) seasonal cumulative DHI (Cum_s), (**b**) decadal maximum DHI (Max_{lt}), (**c**) seasonal minimum DHI (Min_s), (**d**) decadal minimum DHI (Min_{lt}), (**e**) seasonal coefficient of variation DHI (CV_s), and (**f**) decadal coefficient of variation DHI (CV_{lt}). White areas indicate regions with no data, such as urban centers and inland water bodies.

Principal component analysis (PCA) of the six DHI metrics across 10,000 randomly selected global sample pixels revealed that 94.8% of the total variance was explained by the first principal component (PC1), which primarily captured gradients in *available energy* (Figure 7a). PC2 represented a combination of *environmental stability* and *environmental stress* factors, accounting for additional ecological variation. The three-dimensional PCA space demonstrated a clear separation among plant functional types (PFTs). For example, evergreen broadleaf forests (EBF) clustered in the high-productivity, low-variability quadrant—indicating stable, energy-rich environments—while open shrublands (OSH) occupied the opposite extreme of the low-productivity, high-variability space (Figure 7c). This ordination effectively captured the fundamental trade-offs between productivity and environmental variability that characterize global vegetation patterns.

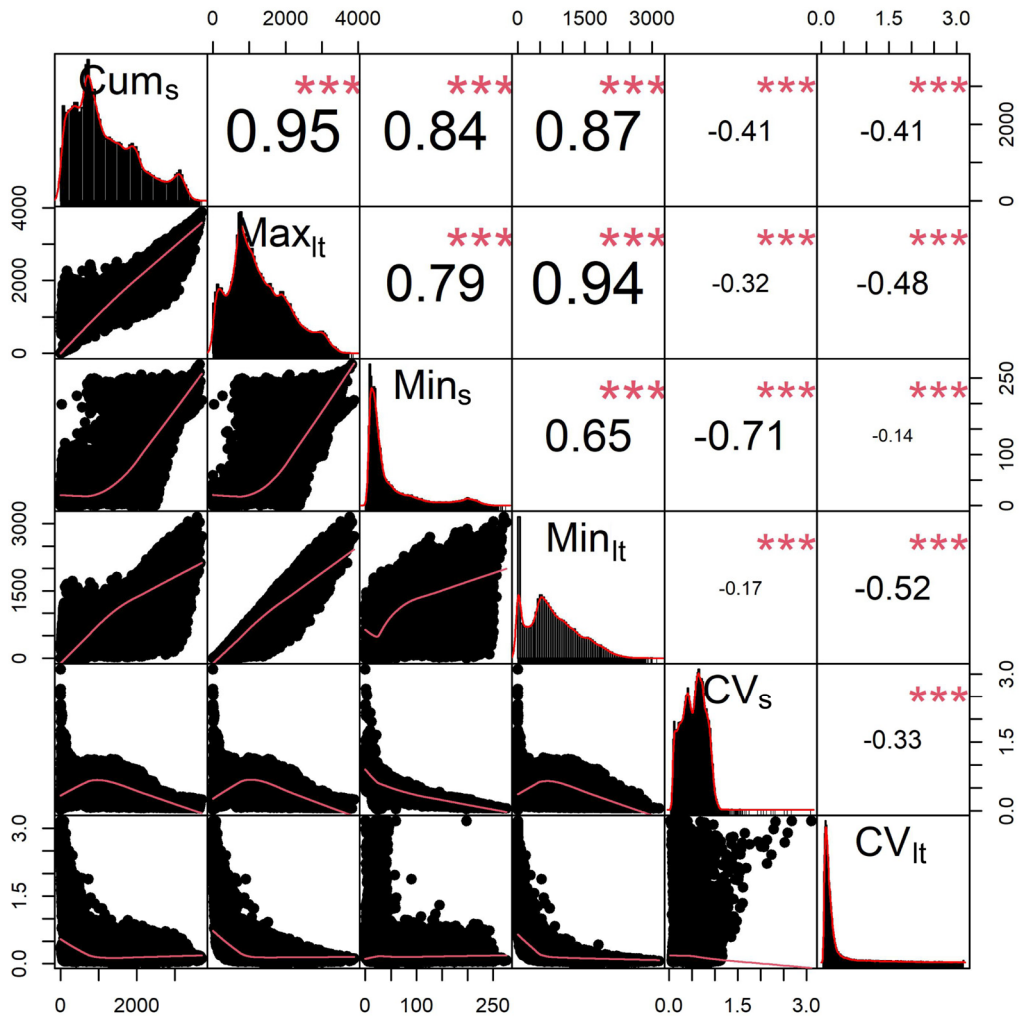


Figure 6. Correlation matrix plot depicting the pairwise relationships among the six GPP_{eLUE}-derived DHI metrics. Diagonal elements display the histogram of each variable to illustrate its data distribution. The lower triangular matrix contains scatter plots (black dots) with red local regression (LOESS) curves to visualize trends between variable pairs. The upper triangular matrix presents Pearson's correlation coefficient (*R*) values, which quantify the linear associations between the variables. Red asterisks denote the level of statistical significance: *** $p < 0.001$ (highly significant).

3.3. Predicting Global Species Richness Using DHIs Metrics and Random Forest Regression

The random forest (RF) regression model exhibited substantial predictive power for global species richness when utilizing the DHI metrics (Figures 8 and 9). Models incorporating either seasonal or long-term metrics alone explained 86% and 80% of the variance (cross-validated R^2, or R^2_{cv}) in species richness across all four combined taxa, respectively (Figure 8c,e). However, the integrated model combining both seasonal and long-term metrics achieved superior performance, explaining 89% of the variance (R^2_{cv} = 0.89) with robust error metrics ($RMSE_{cv}$ = 68.20, MAE_{cv} = 45.62) (Figure 8a).

To quantify the relative contribution of each predictor, we utilized the Percentage Increase in Mean Squared Error (%IncMSE). This metric measures the decline in model predictive accuracy (as defined by MSE) when the values of a specific variable are randomly permuted; consequently, a higher %IncMSE value indicates that the variable is essential for maintaining the model's predictive performance, reflecting its greater ecological importance in structuring global species richness patterns. Variable importance analysis revealed CV_{lt} as the most influential predictor, followed by Min_s, Cum_s, Max_{lt}, CV_s, and Min_{lt} (Figure 8b).

This hierarchical importance highlights the particular significance of inter-annual variability and seasonal minimum productivity in explaining global species richness patterns.

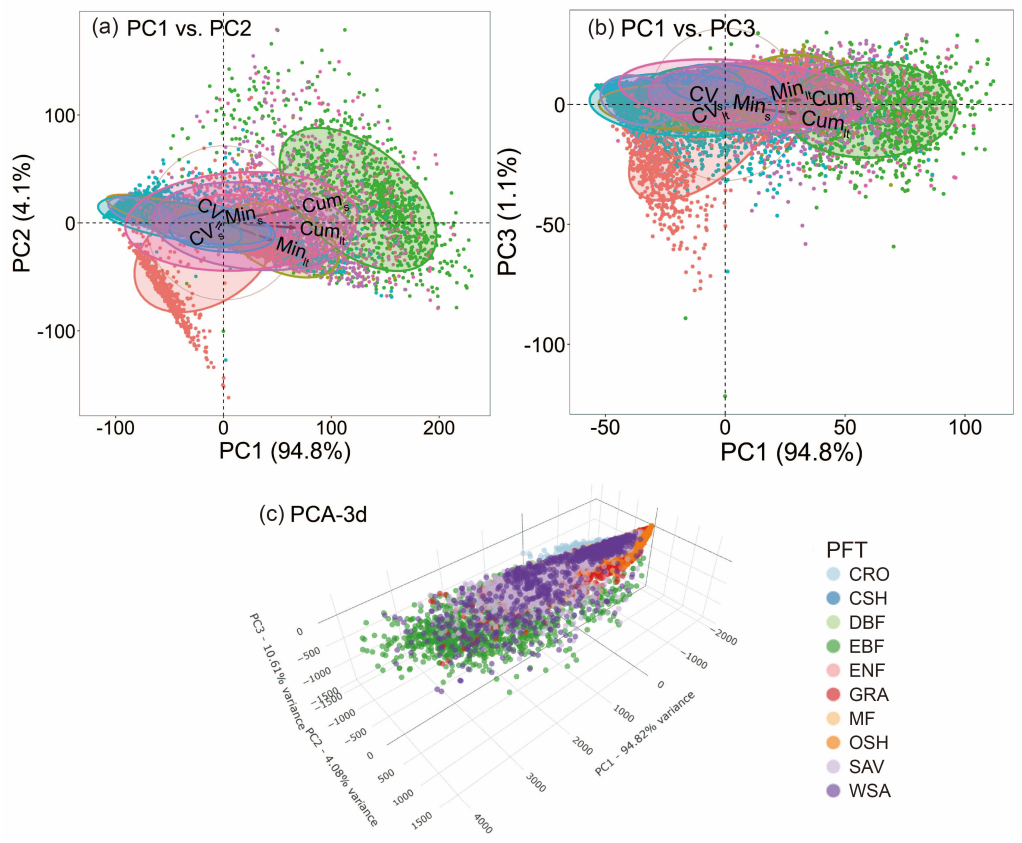


Figure 7. Principal component analysis (PCA) of the six DHI metrics, calculated using 10,000 randomly selected global data points, where each point represents a 0.05° × 0.05° pixel. (**a**) PC1 vs. PC2; (**b**) PC1 vs. PC3; (**c**) three-dimensional (PC1, PC2, PC3) coordinates.

The random forest model demonstrated consistently strong predictive performance across individual taxonomic groups when incorporating the full suite of six DHI metrics. The comprehensive model explained 86% of the variance for amphibians, 85% for both birds and mammals, and 88% for reptiles (Figure 9). For each individual taxon, this integrated six-metric model consistently outperformed alternative configurations that relied solely on seasonal or long-term data (Figures S5–S8). Notably, inter-annual variability (CV_{lt}) emerged as the dominant predictor for birds, mammals, and reptiles, although it showed relatively reduced importance for amphibians. The relative contributions of the remaining metrics exhibited distinct taxon-specific patterns: Min_s was particularly influential for amphibians, whereas Cum_s demonstrated greater importance for endothermic species (Figure 9). These results reinforce the conclusion that different temporal dimensions of productivity exert distinct controls on vertebrate diversity patterns across diverse evolutionary lineages. As illustrated in Figure 9, these patterns highlight significant regional variations in DHI responses; for more detailed comparative assessments across specific biomes and taxonomic groups, please refer to Supplementary Figures S5–S8.

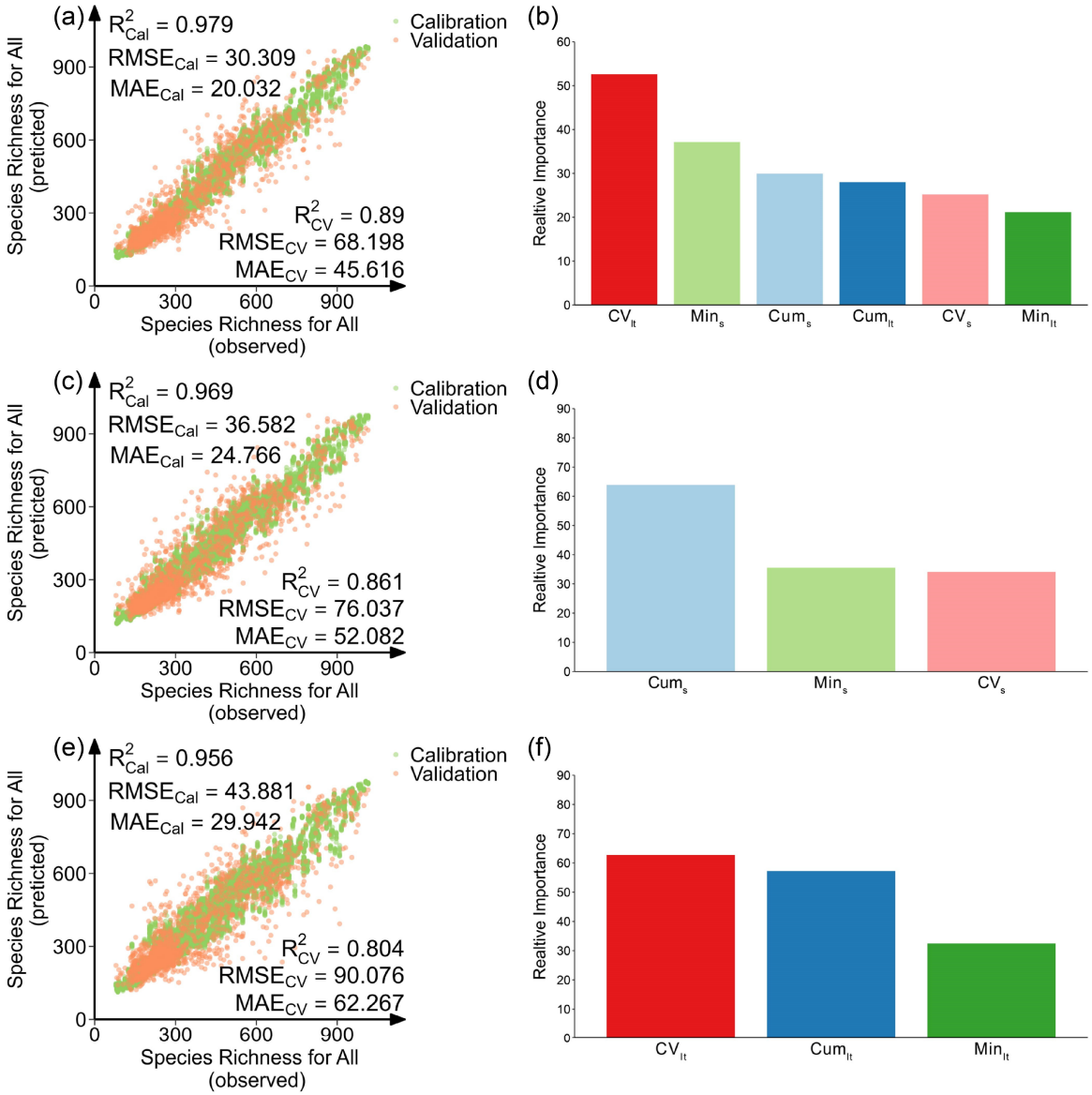


Figure 8. Performance evaluation and variable importance of the random forest regression models for predicting overall global species richness (all taxa combined). Scatterplots depict the model performance using (**a**) all six DHI metrics, (**c**) the three seasonal DHIs only, and (**e**) the three long-term DHIs only. Bar charts (**b**,**d**,**f**) display the corresponding relative variable importance for each model configuration. Subscripts "Cal" and "CV" denote statistical measures derived from the calibration (light green) and cross-validation (light orange) datasets, respectively.

Figure 10 demonstrates that across nearly all vertebrate taxa and biogeographic realms, species richness predictions achieved maximum accuracy when utilizing the comprehensive six-metric model (R^2_{cv} ranging from 0.60 to 0.89). Generally, models utilizing only seasonal metrics outperformed those relying solely on long-term metrics in explaining species richness patterns. A notable exception occurred in the Afrotropical (AT) realm, where long-term metrics provided superior predictive power compared to seasonal indices, suggesting the presence of unique ecological drivers of biodiversity in this region. These results highlight how the relative importance of seasonal versus inter-annual productivity dynamics varies geographically, while simultaneously confirming that integrating both temporal dimensions consistently yields optimal predictions across diverse ecosystems.

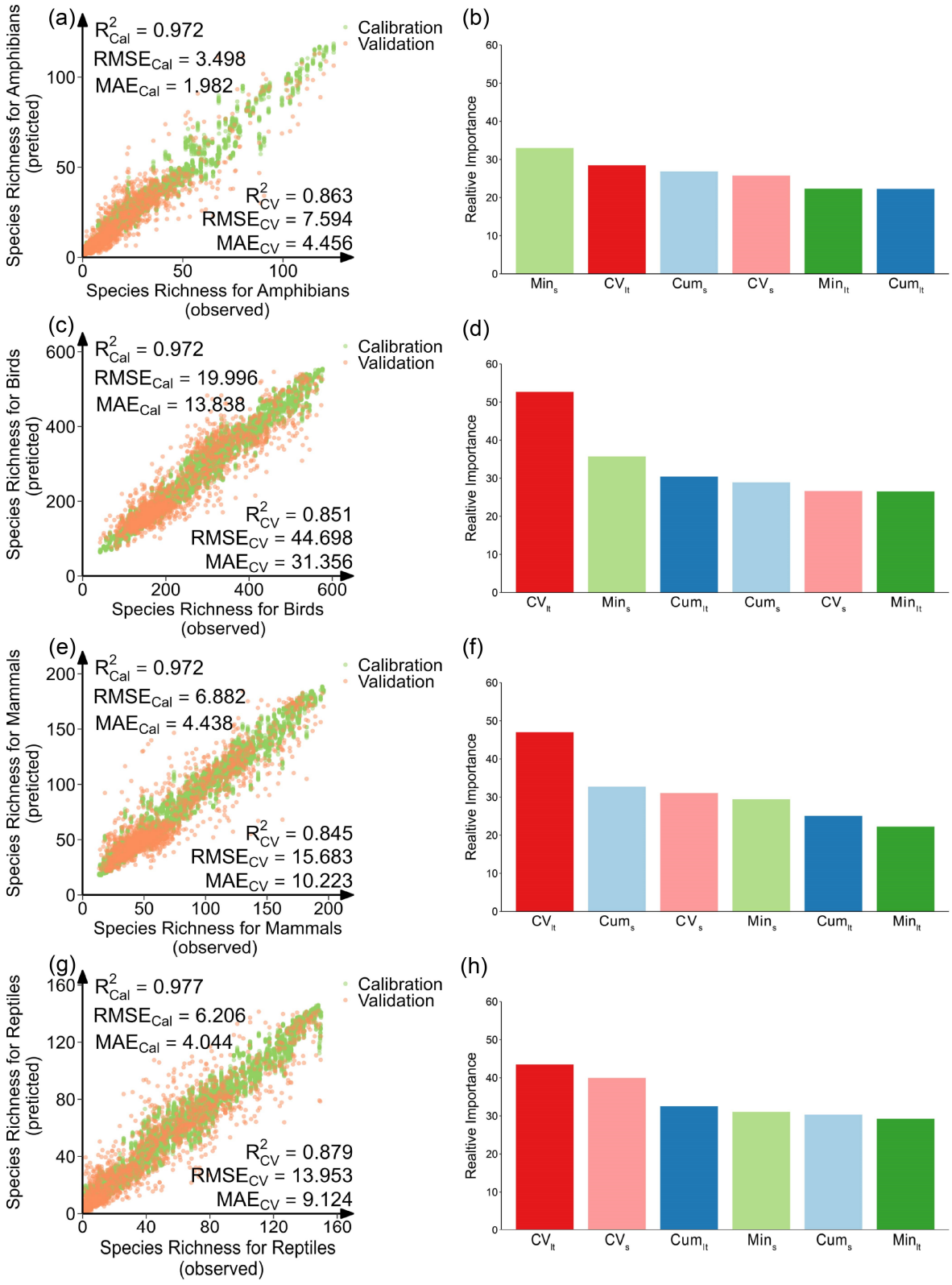


Figure 9. Performance evaluation and variable importance of the comprehensive six-metric random forest models for individual taxonomic groups. Scatterplots display the predictive performance for (**a**) amphibians, (**c**) birds, (**e**) mammals, and (**g**) reptiles. Corresponding bar charts (**b**,**d**,**f**,**h**) illustrate the relative variable importance of the six DHI metrics for each respective taxon.

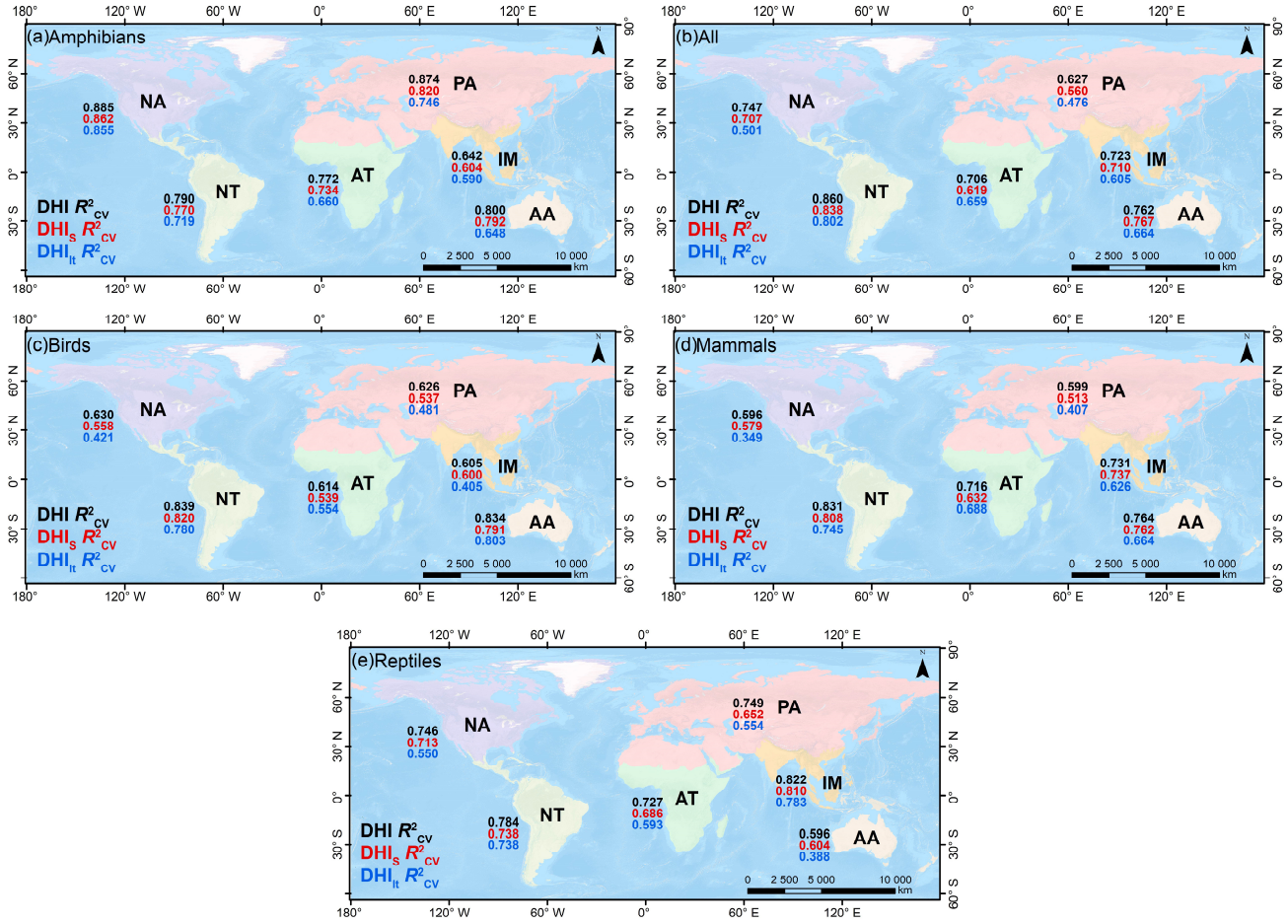


Figure 10. Random forest model performance (cross-validated R^2, or R^2_{cv}) for predicting the species richness of individual taxa (**a**–**d**) and all taxa combined (**e**) across six biogeographic realms. Text colors indicate the predictor sets used: all six DHIs (black), the three seasonal DHIs only (red), and the three long-term DHIs only (blue).

The random forest model's prediction of global species richness closely corresponds to established IUCN Red List patterns while revealing enhanced spatial granularity (Figure 11). The model accurately identifies tropical zones—including the Amazon Basin, Central Africa, and Southeast Asia—as biodiversity hotspots harboring maximum richness values, contrasting sharply with the species-poor high-latitude regions. Notably, the predicted temporal variability in richness (Figure 11, right panels) exhibits a proportional positive relationship with absolute richness, where tropical hotspots display substantial temporal fluctuations (SD = 22.5–30) compared to the stable but depauperate polar regions (SD = 0–7.5). This pattern likely reflects the greater ecological complexity and dynamic nature of tropical ecosystems, where higher species turnover and heightened sensitivity to inter-annual climate variations may drive increased temporal variability in richness estimates. The model's capacity to simultaneously capture spatial gradients and temporal dynamics highlights its robust utility for identifying conservation priorities across varying biogeographic contexts.

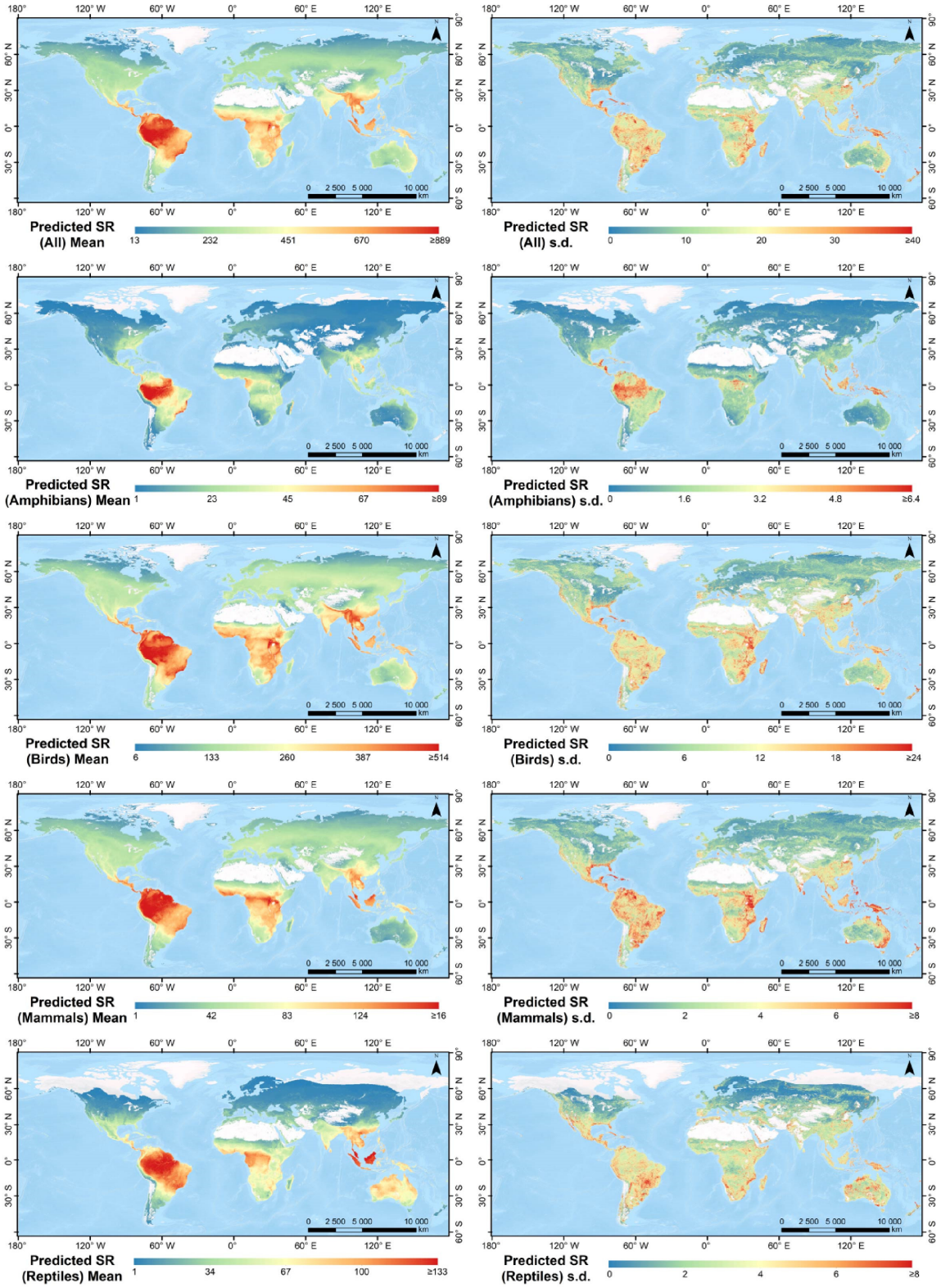


Figure 11. Spatial distribution of predicted global species richness (SR) for amphibians, birds, mammals, and reptiles, modeled using the random forest algorithm based on the six DHI metrics. Left panels display the mean predicted species richness derived across 15 annual time-series inputs, while right panels show the standard deviation (SD) of these predictions. SR is defined as the number of species occurring per grid cell. The SD represents the inter-annual variability in predicted richness across the evaluated temporal scenarios.

Furthermore, the spatial distribution of the Standard Deviation (SD) of predicted richness (Figure 11, right panel) reveals distinct geographic patterns of inter-annual fluctuation. Notably, the highest SD values are heavily concentrated within global biodiversity hotspots, particularly across the Amazon Basin, the Congo Basin, and Southeast Asia. This indicates substantial year-to-year variability in the predicted species richness across these equatorial regions compared to higher latitudes.

4. Discussion

4.1. Bridging Satellite Remote Sensing and Biodiversity Conservation Using Extended Dynamic Habitat Indices (DHIs)

In this study, we developed an extended Dynamic Habitat Indices (DHIs) framework by formally integrating seasonal (Cum_s, Min_s, CV_s) and long-term (Max_{lt}, Min_{lt}, CV_{lt}) productivity metrics. This integration significantly improves the prediction of global faunal species richness patterns. By explaining 89% of the variance in cumulative vertebrate species richness, the integrated model demonstrates the framework's robustness in transforming raw satellite observations into ecologically meaningful indices for macroscopic conservation planning [16–18].

The satellite-derived DHIs leverage consistent, long-term MODIS observations and the robust GPP_{eLUE} productivity model. This combination provides a high-resolution mapping capability that is essential for identifying ecological transition zones and tracking conservation outcomes over decadal scales. Furthermore, the mathematical simplicity of the DHI framework ensures its inherent scalability—from local ecosystem assessments to global-scale applications [47,48]. This functional scalability makes the enhanced DHI suite particularly valuable for optimizing protected area networks and evaluating global progress toward international biodiversity targets.

Our random forest modeling reveals that the relationships between DHIs and species richness exhibit contextual, nonlinear thresholds [17,49]. Notably, inter-annual productivity variability (CV_{lt}) emerged as the most influential predictor across most taxa, strongly underscoring *environmental stability* as a dominant mechanism shaping macroecological biodiversity patterns. The model not only successfully identifies established richness hotspots but also detects biodiversity-sensitive zones by mapping patterns of temporal vulnerability. This dual capacity—capturing both spatial richness gradients and temporal vulnerability trends—provides an unprecedented tool for anticipating conservation priorities in rapidly changing environments. Consequently, this study advances DHIs beyond simple productivity proxies, establishing them as robust indicators of habitat quality and broader ecosystem resilience.

While we acknowledge the high spatial multicollinearity among certain productivity indices (e.g., the strong correlation between Cum_s and Max_{lt}), retaining these collinear metrics is theoretically imperative for the completeness of the extended DHI framework. Statistical co-variation across macroecological scales does not equate to ecological redundancy; rather, these metrics parameterize fundamentally distinct environmental constraints acting on species life-history strategies. Specifically, Cum_s quantifies the baseline intra-annual energy flux required to sustain regular seasonal reproduction and population maintenance. In contrast, Max_{lt} captures the decadal peak of available energy, explicitly defining the absolute upper ceiling of ecosystem carrying capacity over a long-term period. Similarly, while seasonal minimums (Min_s) reflect regular low-productivity periods, the decadal minimum (Min_{lt}) establishes the ultimate multi-year survival bottleneck, dictating species persistence during extreme, episodic resource scarcity. Removing these long-term extremes based solely on statistical collinearity would sacrifice critical ecological mechanisms—namely, the absolute resource ceilings and the most severe environmen-

tal filters structuring global biodiversity. Furthermore, as confirmed by our Recursive Feature Elimination (RFE) and LASSO regression analyses (Table S2), the Random Forest framework is inherently robust to this shared variance. This allows the model to leverage these distinct ecological nuances without compromising stability, thereby preserving the structural dominance of inter-annual variability (CV_{lt}) as the primary constraint on global vertebrate richness.

While the traditional seasonal DHIs already provide a strong baseline for predicting global species richness, the integration of long-term metrics elevates the model beyond mere statistical refinement. Although the absolute increase in R^2 (e.g., R^2 improving from 0.86 to 0.89) might seem numerically incremental, it effectively reduces the unexplained variance by approximately 21%. More importantly, the primary value of this six-dimensional framework lies in mechanistic discovery rather than purely maximizing predictive power. By maintaining a highly parsimonious model structure (only six predictors), the framework explicitly revealed that inter-annual environmental stability (CV_{lt}) supersedes seasonal baseline productivity as the dominant macroecological constraint. This theoretical recalibration—highlighting stability-mediated persistence over average resource availability—provides profound ecological significance that strongly justifies the inclusion of long-term temporal dynamics.

4.2. Incorporating Inter-Annual Variability Enhances the Predictability of Global Species Richness Patterns

The three long-term indices (Max_{lt}, Min_{lt}, CV_{lt}) extend the traditional DHI framework by capturing critical inter-annual productivity dynamics. Max_{lt} enhances the *available energy* hypothesis by identifying the decadal peak carrying capacity, thereby complementing Cum_s. Similarly, Min_{lt} strengthens the *environmental stress* hypothesis by establishing multi-year minimum productivity thresholds. Most significantly, CV_{lt} quantifies inter-annual variability as a core component of *environmental stability* [25], revealing critical habitat fluctuations that remain undetected in purely seasonal data. Collectively, these long-term indices add essential temporal depth to biodiversity assessments, particularly in ecosystems strongly structured by climate variability and disturbance regimes [50,51].

Although seasonal indices alone explain substantial variance in species distributions, incorporating long-term dynamics provides complementary ecological information that significantly boosts overall model performance. While recent applications have demonstrated that calculating traditional DHIs on an annual basis can effectively capture temporal variance in bird species richness at regional scales [32], our framework extends this temporal perspective to a global scale. By integrating decadal extremes and inter-annual variability alongside seasonal metrics, the six-dimensional DHI suite captures long-term resource bottlenecks and climate fluctuations within a unified model, providing a robust alternative to analyzing discrete annual slices or incorporating additional climatic covariates. Within this integrated framework, our machine learning analysis reveals a nuanced hierarchy among the foundational ecological hypotheses: while *available energy* (Cum_s) and *environmental stress* (Min_s) exhibit strong bivariate correlations with species richness, *environmental stability* (CV_{lt}) emerges as the single most influential predictor. This seemingly counter-intuitive finding—where inter-annual variability surpasses mean productivity metrics in predictive importance—highlights how long-term fluctuations disproportionately dictate habitat quality and species persistence [25,27]. Ecologically, while seasonal metrics (such as Cum_s and Min_s) establish the baseline carrying capacity and regular stress thresholds, CV_{lt} captures the long-term resource volatility and the frequency of unpredictable environmental bottlenecks (e.g., severe multi-year droughts or climate extremes). The underlying mechanism is that species persistence is ultimately constrained by these episodic, severe resource fluctuations. Even in environments with high average productivity, high inter-

annual volatility leads to stability-mediated local extinctions, acting as a supreme ecological filter that prevents species from maintaining viable populations over time. This paradox likely arises because CV_{lt} effectively captures stability-mediated extinction risks driven by species' nonlinear responses to resource volatility and its interactive effects with other productivity dimensions [52]. It is noteworthy that while inter-annual variability (CV_{lt}) exhibits a relatively weak bivariate linear correlation with species richness, it emerges as the most influential predictor within the Random Forest framework. This highlights the limitation of assuming simple linear relationships in macroecology. CV_{lt} predominantly acts as a non-linear, conditional environmental filter; for instance, high inter-annual volatility strongly penalizes biodiversity even in regions with high mean productivity (Cum_s). The machine learning framework successfully captures these complex multidimensional interactions and threshold effects, demonstrating that long-term habitat stability dictates species persistence in ways that traditional bivariate linear correlations fundamentally fail to detect. Consequently, this finding fundamentally recalibrates our understanding of the mechanisms linking primary productivity to global richness patterns.

Furthermore, the integration of inter-annual dynamics capitalizes on rapidly expanding satellite Earth observation capabilities across increasingly fine spatial resolutions [53]. This enhanced temporal dimension facilitates the investigation of extreme climate legacy effects [54], decadal greening trends, and cascading hydrological impacts on ecosystem functioning. Given that climate extremes drive the majority of inter-annual GPP variability and are projected to increase in frequency, metrics like CV_{lt} will become increasingly vital for continuously monitoring habitat stability. Ultimately, satellite remote sensing provides an unparalleled capacity to capture these dynamic biodiversity constraints across multiple temporal scales, serving as a powerful, synoptic complement to traditional ground-based field observations.

4.3. Limitations and Future Perspectives

While satellite-derived DHIs provide highly scalable predictions of species richness, their absolute accuracy fundamentally depends on the quality of in situ biodiversity data used for calibration [55,56]. Current analyses often rely on IUCN Red List distribution maps [57,58], which tend to overestimate actual species occurrences due to habitat-based range extrapolations [18,59]. This limitation often necessitates spatial aggregation to coarser resolutions to ensure statistical reliability. Future efforts must prioritize integrating direct occurrence records from global and regional biodiversity databases, although this will require addressing persistent gaps in data quality, sampling bias, and spatiotemporal consistency [60,61]. Furthermore, our current analytical framework is taxonomically restricted to terrestrial vertebrates. The lack of validation against plant and invertebrate taxa—which constitute the vast majority of global biodiversity and possess fundamentally different life-history strategies, dispersal capacities, and physiological tolerances—limits the generalizability of our findings to other biological groups. For instance, the relative importance of inter-annual environmental stability (CV_{lt}) versus mean energy availability (Max_{lt}) may vary significantly for organisms capable of extended dormancy or diapause. Expanding the DHI framework to include high-resolution global distribution data for flora and invertebrate fauna remains a critical frontier for future macroecological research to achieve a truly holistic understanding of global biodiversity dynamics.

An inherent methodological challenge in macroecological modeling is the temporal mismatch between species richness snapshots and multi-year environmental observations. Our analytical framework implicitly operates under the 'temporal quasi-equilibrium' hypothesis. Large-scale species richness gradients are primarily governed by evolutionary history and long-term climatic constraints; thus, they exhibit robust temporal stability and

remain relatively insensitive to short-term, inter-annual population fluctuations [62,63]. Consequently, a single-year species richness snapshot (e.g., 2004) effectively integrates these historical legacies and reflects the contemporary spatial distribution of biodiversity. To match this stable biological pattern, we utilized a multi-year baseline (e.g., 2001–2010) to derive our long-term DHIs. This approach aligns with the core principles of the Species-Energy Theory [21], as it captures the stable 'climatological productivity regime'—the long-term average and inter-annual variability of habitat carrying capacity—while filtering out the stochastic noise of transient annual anomalies [64]. Future multi-decadal biodiversity monitoring initiatives will be crucial to transition from spatial pattern matching to true spatiotemporal dynamic tracking.

Furthermore, the assessment of multi-decadal habitat dynamics—which is critical for understanding long-term population-level processes—remains challenging with current satellite datasets. Although existing Earth observation records span over 50 years, high-resolution continuous observations capturing century-scale ecological processes remain inadequate. However, emerging initiatives aimed at harmonizing the Landsat archive into consistent global products [53], coupled with planned next-generation missions (e.g., Landsat Next) [65,66] and commitments from international space agencies, promise to bridge this gap. These advancements will soon enable robust analyses of habitat-biodiversity relationships across true generational timescales.

Although our enhanced framework incorporates inter-annual variability, it does not currently explicitly isolate the impacts of severe climate extremes or discrete disturbance events, which are increasingly recognized as critical drivers of habitat degradation under climate change [67,68]. Because these episodic events can induce lasting ecological legacy effects [69,70] and are projected to intensify globally [71], integrating specific disturbance regimes into future DHI frameworks is imperative for maintaining predictive accuracy under rapidly shifting global change scenarios [72].

Importantly, the structural resilience of this extended DHI framework is empirically robust against episodic climate cycles. To validate this, we conducted a comprehensive sensitivity analysis across varying temporal baselines—including an initial baseline decade (2001–2010), an ENSO-inclusive decade (2011–2020), and extended 15-year (2001–2015) and 20-year (2001–2020) continuous windows. This analysis demonstrated remarkable model stability. Across all tested periods, the overall predictive accuracy remained invariant ($R^2 \approx 0.81$), and CV_{lt} consistently maintained its position as the paramount environmental predictor (Supplementary Figure S10). This confirms that our framework intrinsically captures the macroecological consequences of inter-annual climatic volatility without overfitting to a specific observational baseline.

Finally, the reliability of DHIs is inherently constrained by uncertainties in the underlying satellite-derived GPP products, stemming from sensor artifacts and algorithmic assumptions [73]. These uncertainties are particularly acute for inter-annual variability metrics (e.g., CV_{lt}), as current global GPP products often exhibit poor consensus when quantifying year-to-year productivity fluctuations [74,75].

The elevated Standard Deviation (SD) of predicted richness observed in tropical hotspots (e.g., the Amazon, Congo Basin, and Southeast Asia; Figure 11) warrants careful interpretation, as it likely reflects a synergistic combination of genuine ecological dynamics and inherent model uncertainty. Ecologically, these hyper-diverse regions are frequently subjected to severe inter-annual climatic oscillations, such as the El Niño-Southern Oscillation (ENSO), which trigger substantial temporal pulses and deficits in primary productivity. Consequently, the high SD captures the real, transient fluctuations in the environmental carrying capacity that govern local resource availability. However, from a statistical and modeling standpoint, this high SD also encapsulates predictive uncertainty. Mathemat-

ically, areas with a higher absolute baseline of species inherently tend to exhibit larger absolute variance. Furthermore, in these structurally complex and species-saturated equatorial ecosystems, the macroecological relationship between primary productivity and species richness becomes highly non-linear and occasionally decoupled. In such saturated environments, the Random Forest model experiences greater extrapolation uncertainty. Recognizing this dual driver—genuine climatic volatility intertwined with modeling uncertainty at high-diversity extremes—is critical for properly interpreting these predictive variance maps in the context of conservation prioritization.

Finally, a post hoc spatial diagnostic reveals that our satellite-derived DHIs successfully absorb a substantial proportion of the spatial variance governed by environmental gradients. Specifically, the exceptionally high baseline spatial autocorrelation of raw global species richness (Global Moran's I = 0.9736) was reduced by 35.6% in our model predictions (Residual Global Moran's I = 0.6266). This remaining residual structure largely reflects intrinsic historical processes (e.g., dispersal limitations, evolutionary history, and biogeographic barriers) rather than contemporary environmental overfitting. Crucially, a Local Moran's I (LISA) analysis confirms that this remaining autocorrelation is not driven by systematic prediction bias in data-sparse biomes. Globally, 80.8% of the prediction residuals exhibit no significant spatial clustering ($p > 0.05$; Figure S9). In extreme environments specifically highlighted as data-sparse, such as high-latitude regions (>50°), only 1.5% of the grids show significant residual autocorrelation. Instead, the localized clustering is predominantly concentrated in hyper-diverse tropical rainforests (e.g., the Amazon and Southeast Asia). This localized pattern corroborates our previous observation regarding predictive uncertainty in structurally complex ecosystems, further indicating that residual clustering stems from saturation effects in species-rich environments rather than a failure in broad-scale environmental extrapolation. Future macroecological modeling efforts should consider integrating explicit spatial error models to further disentangle these deep-time evolutionary legacies from contemporary environmental constraints.

To overcome these limitations, we propose three key research priorities for advancing biodiversity monitoring: (1) integrating multi-source satellite archives with emerging high-resolution sensors to construct long-term, fine-scale habitat datasets; (2) developing composite indices that explicitly quantify ecosystem disturbances for seamless integration into the DHI framework; and (3) advancing GPP modeling through next-generation Earth observation missions to improve the precision of primary productivity estimates, with a specific focus on reconciling inter-annual variability metrics.

5. Conclusions

This study successfully extended the traditional Dynamic Habitat Indices (DHI) framework by formally integrating both seasonal and long-term productivity variations, establishing a comprehensive six-dimensional index system to better predict global species richness. Our results demonstrate that incorporating long-term DHIs—specifically decadal maximum productivity, decadal minimum productivity, and inter-annual variability—significantly improves overall predictive performance. Notably, the integrated random forest model achieved a cross-validated R^2_{cv} of 0.89 for cumulative species richness across four major terrestrial vertebrate taxa. Within this enhanced framework, inter-annual productivity variability (CV_{lt}) emerged as the single most influential predictor, fundamentally underscoring the critical role of *environmental stability* in shaping macroecological biodiversity patterns. Furthermore, this study highlights the synergistic, complementary roles of intra-annual and inter-annual productivity dynamics: while seasonal DHIs reflect immediate baseline habitat conditions, long-term DHIs capture broader ecological trends, extreme resource limitations, and temporal volatility. Ultimately, this extended

DHI framework provides a robust, scalable approach for understanding and predicting species richness patterns across the globe, effectively bridging satellite remote sensing with macroecological research to address the escalating biodiversity crisis.

Supplementary Materials: The following supporting information can be downloaded at: https://www.mdpi.com/article/10.3390/rs18132085/s1. References [76–118] are cited in the Supplementary Materials.

Author Contributions: X.M. conceived the ideas and designed methodology; K.L. (Kedi Liu) and C.C. collected the data; X.M., K.L. (Kedi Liu), K.L. (Kaiyue Luo) and Y.L. analyzed the data; X.M. and K.L. (Kedi Liu) led the writing of the manuscript. All authors have read and agreed to the published version of the manuscript.

Funding: This work was supported by the Open Fund of the State Key Laboratory of Herbage Improvement and Grassland Agro-ecosystems (SKLHIGA202504), Natural Science Foundation of Gansu Province, China (25JRRA646); the Fengyun Application Pioneering Project of the National Satellite Meteorology Center (FY-APP-2024.0302).

Data Availability Statement: The gross primary productivity (GPP) dataset used in this study was derived from the publicly available GPPeLUE product, available through the Dryad Digital Repository (https://doi.org/10.5061/dryad.v9s4mw74h, accessed on 14 June 2026). Eddy-covariance flux tower measurements used for validation were obtained from the FLUXNET2015 database (https://fluxnet.org/data/fluxnet2015-dataset/, accessed on 14 June 2026). Global terrestrial vertebrate species richness data were obtained from the IUCN spatial datasets (https://www.iucnredlist.org/resources/other-spatial-downloads, accessed on 14 June 2026). Biogeographic realm boundaries were derived from the WWF Terrestrial Ecoregions dataset (https://www.worldwildlife.org/biomes, accessed on 14 June 2026). All datasets analyzed in this study are publicly available from the corresponding repositories and data portals cited above. No new observational datasets were generated in this study. Processed data supporting the findings of this study are available from the corresponding author upon reasonable request (xlma@lzu.edu.cn).

Conflicts of Interest: The authors declare no conflict of interest.

References

1. Koh, L.P.; Dunn, R.R.; Sodhi, N.S.; Colwell, R.K.; Proctor, H.C.; Smith, V.S. Species coextinctions and the biodiversity crisis. *Science* **2004**, *305*, 1632–1634. [CrossRef] [PubMed]
2. Pörtner, H.-O.; Scholes, R.J.; Arneth, A.; Barnes, D.K.A.; Burrows, M.T.; Diamond, S.E.; Duarte, C.M.; Kiessling, W.; Leadley, P.; Managi, S.; et al. Overcoming the coupled climate and biodiversity crises and their societal impacts. *Science* **2023**, *380*, eabl4881. [CrossRef] [PubMed]
3. Cardinale, B.J.; Duffy, J.E.; Gonzalez, A.; Hooper, D.U.; Perrings, C.; Venail, P.; Narwani, A.; Mace, G.M.; Tilman, D.; Wardle, D.A.; et al. Biodiversity loss and its impact on humanity. *Nature* **2012**, *486*, 59–67. [CrossRef] [PubMed]
4. Pereira, H.M.; Martins, I.S.; Rosa, I.M.D.; Kim, H.; Leadley, P.; Popp, A.; van Vuuren, D.P.; Hurtt, G.; Quoss, L.; Arneth, A.; et al. Global trends and scenarios for terrestrial biodiversity and ecosystem services from 1900 to 2050. *Science* **2024**, *384*, 458–465. [CrossRef] [PubMed]
5. Meyer, C.; Kreft, H.; Guralnick, R.; Jetz, W. Global priorities for an effective information basis of biodiversity distributions. *Nat. Commun.* **2015**, *6*, 8221. [CrossRef] [PubMed]
6. Geijzendorffer, I.R.; Regan, E.C.; Pereira, H.M.; Brotons, L.; Brummitt, N.; Gavish, Y.; Haase, P.; Martin, C.S.; Mihoub, J.-B.; Secades, C.; et al. Bridging the gap between biodiversity data and policy reporting needs: An Essential Biodiversity Variables perspective. *J. Appl. Ecol.* **2016**, *53*, 1341–1350.
7. Migliavacca, M.; Grassi, G.; Bastos, A.; Ceccherini, G.; Ciais, P.; Janssens-Maenhout, G.; Lugato, E.; Mahecha, M.D.; Novick, K.A.; Peñuelas, J.; et al. Securing the forest carbon sink for the European Union's climate ambition. *Nature* **2025**, *643*, 1203–1213. [CrossRef] [PubMed]
8. Mollot, G.; Pantel, J.H.; Romanuk, T.N. The effects of invasive species on the decline in species richness: A global meta-analysis. In *Advances in Ecological Research*; Bohan, D.A., Dumbrell, A.J., Massol, F., Eds.; Academic Press: Cambridge, MA, USA, 2017; pp. 61–83.

9. Rose, R.A.; Byler, D.; Eastman, J.R.; Fleishman, E.; Geller, G.; Goetz, S.; Guild, L.; Hamilton, H.; Hansen, M.; Headley, R. Ten ways remote sensing can contribute to conservation. *Conserv. Biol.* **2015**, *29*, 350–359. [PubMed]
10. Ma, X.; Migliavacca, M.; Wirth, C.; Bohn, F.J.; Huth, A.; Richter, R.; Mahecha, M.D. Monitoring plant functional diversity using the reflectance and echo from space. *Remote Sens.* **2020**, *12*, 1248. [CrossRef]
11. Perpinyà-Vallès, M.; Machefer, M.; Ameztegui, A.; Escorihuela, M.J.; Brandt, M.; Romero, L. Quantification of carbon stocks at the individual tree level in semi-arid regions in Africa. *J. Remote Sens.* **2024**, *4*, 0359.
12. Schweiger, A.K.; Cavender-Bares, J.; Townsend, P.A.; Hobbie, S.E.; Madritch, M.D.; Wang, R.; Tilman, D.; Gamon, J.A. Plant spectral diversity integrates functional and phylogenetic components of biodiversity and predicts ecosystem function. *Nat. Ecol. Evol.* **2018**, *2*, 976–982. [CrossRef] [PubMed]
13. Ma, X.; Mahecha, M.D.; Migliavacca, M.; van der Plas, F.; Benavides, R.; Ratcliffe, S.; Kattge, J.; Richter, R.; Musavi, T.; Baeten, L.; et al. Inferring plant functional diversity from space: The potential of Sentinel-2. *Remote Sens. Environ.* **2019**, *233*, 111368. [CrossRef]
14. Wang, R.; Gamon, J.A. Remote sensing of terrestrial plant biodiversity. *Remote Sens. Environ.* **2019**, *231*, 111218. [CrossRef]
15. Mackey, B.; Bryan, J.; Randall, L. Australia's Dynamic Habitat Template for 2003. In Proceedings of the MODIS Vegetation Workshop II, Missoula, MT, USA, 17–19 August 2004.
16. Liu, K.; Cao, C.; Gao, S.; Yang, W.; Ma, X. Bridging satellite productivity and global biodiversity: Unveiling insights through dynamic habitat indices. *J. Remote Sens.* **2025**, *5*, 624. [CrossRef]
17. Coops, N.C.; Bolton, D.K.; Hobi, M.L.; Radeloff, V.C. Untangling multiple species richness hypothesis globally using remote sensing habitat indices. *Ecol. Indic.* **2019**, *107*, 105567. [CrossRef]
18. Radeloff, V.C.; Dubinin, M.; Coops, N.C.; Allen, A.M.; Brooks, T.M.; Clayton, M.K.; Costa, G.C.; Graham, C.H.; Helmers, D.P.; Ives, A.R.; et al. The Dynamic Habitat Indices (DHIs) from MODIS and global biodiversity. *Remote Sens. Environ.* **2019**, *222*, 204–214. [CrossRef]
19. Liu, D.; Silveira, E.M.O.; Razenkova, E.; Anand, A.; Dubinin, M.; Hobi, M.; Pidgeon, A.M.; Radeloff, V.C. Global dynamic habitat indices (DHIs) based on MODIS and VIIRS vegetation products. *Remote Sens. Environ.* **2026**, *332*, 115099.
20. Wright, D.H. Species-energy theory: An extension of species-area theory. *Oikos* **1983**, *41*, 496–506.
21. Currie, D.J. Energy and large-scale patterns of animal-and plant-species richness. *Am. Nat.* **1991**, *137*, 27–49.
22. Rohde, K. Latitudinal gradients in species diversity: The search for the primary cause. *Oikos* **1992**, *65*, 514–527. [CrossRef]
23. Mason, N.W.H.; Lanoiselée, C.; Mouillot, D.; Wilson, J.B.; Argillier, C. Does niche overlap control relative abundance in French lacustrine fish communities? A new method incorporating functional traits. *J. Anim. Ecol.* **2008**, *77*, 661–669. [CrossRef] [PubMed]
24. Fjeldsaå, J.; Lovett, J.C. Biodiversity and environmental stability. *Biodivers. Conserv.* **1997**, *6*, 315–323. [CrossRef]
25. Gardner, A.S.; Gaston, K.J.; Maclean, I.M.D. Accounting for inter-annual variability alters long-term estimates of climate suitability. *J. Biogeogr.* **2021**, *48*, 1960–1971.
26. Perez-Navarro, M.A.; Broennimann, O.; Esteve, M.A.; Moya-Perez, J.M.; Carreño, M.F.; Guisan, A.; Lloret, F. Temporal variability is key to modelling the climatic niche. *Divers. Distrib.* **2021**, *27*, 473–484.
27. Berti, E.; Rosenbaum, B.; Reuman, D.C. The impacts of climate variability on the niche concept and distributions of species. *bioRxiv* **2024**. [CrossRef]
28. Briscoe, N.J.; Kearney, M.R.; Taylor, C.A.; Wintle, B.A. Unpacking the mechanisms captured by a correlative species distribution model to improve predictions of climate refugia. *Glob. Change Biol.* **2016**, *22*, 2425–2439. [CrossRef] [PubMed]
29. Vasseur, D.A.; DeLong, J.P.; Gilbert, B.; Greig, H.S.; Harley, C.D.G.; McCann, K.S.; Savage, V.; Tunney, T.D.; O'Connor, M.I. Increased temperature variation poses a greater risk to species than climate warming. *Proc. R. Soc. B Biol. Sci.* **2014**, *281*, 20132612. [CrossRef] [PubMed]
30. Maxwell, S.L.; Butt, N.; Maron, M.; McAlpine, C.A.; Chapman, S.; Ullmann, A.; Segan, D.B.; Watson, J.E.M. Conservation implications of ecological responses to extreme weather and climate events. *Divers. Distrib.* **2018**, *25*, 613–625. [CrossRef]
31. Maron, M.; McAlpine, C.A.; Watson, J.E.M.; Maxwell, S.; Barnard, P. Climate-induced resource bottlenecks exacerbate species vulnerability: A review. *Divers. Distrib.* **2015**, *21*, 731–743.
32. Hobi, M.L.; Farwell, L.S.; Dubinin, M.; Kolesov, D.; Pidgeon, A.M.; Coops, N.C.; Radeloff, V.C. Patterns of bird species richness explained by annual variation in remotely sensed Dynamic Habitat Indices. *Ecol. Indic.* **2021**, *127*, 107774. [CrossRef]
33. Ónodi, G.; Kertész, M.; Bede-Fazekas, Á.; Batáry, P.; Kröel-Dulay, G.; Botta-Dukát, Z. Decline in plant species richness with a chronic decrease of precipitation: The mediating role of the dominant species. *J. Ecol.* **2025**, *113*, 621–634. [CrossRef]
34. Ma, X.; Cao, C.; Yang, W.; Yan, K.; Liu, F.; Wang, Y.; Huete, A. *eLUE-GPP (MODIS): A Global Gross Primary Productivity Product Based on Ecosystem Light-Use-Efficiency Model and MODIS EVI [Dataset]*; Dryad: Durham, NC, USA, 2024. [CrossRef]
35. Ma, X.; Huete, A.; Yu, Q.; Restrepo-Coupe, N.; Beringer, J.; Hutley, L.B.; Kanniah, K.D.; Cleverly, J.; Eamus, D. Parameterization of an ecosystem light-use-efficiency model for predicting savanna GPP using MODIS EVI. *Remote Sens. Environ.* **2014**, *154*, 253–271.
36. Cao, C.; Ma, X.; Yang, W.; Yan, K.; Liu, F.; Wang, Y.; Huete, A. Global upscaling of gross primary productivity using a simple and robust modeling scheme. *IEEE Trans. Geosci. Remote Sens.* **2025**, *63*, 1–13. [CrossRef]

37. Joiner, J.; Yoshida, Y.; Zhang, Y.; Duveiller, G.; Jung, M.; Lyapustin, A.; Wang, Y.; Tucker, C.J. Estimation of terrestrial global gross primary production (GPP) with satellite data-driven models and eddy covariance flux data. *Remote Sens.* **2018**, *10*, 1346. [CrossRef]
38. Lasslop, G.; Reichstein, M.; Papale, D.; Richardson, A.D.; Arneth, A.; Barr, A.; Stoy, P.; Wohlfahrt, G. Separation of net ecosystem exchange into assimilation and respiration using a light response curve approach: Critical issues and global evaluation. *Glob. Change Biol.* **2010**, *16*, 187–208.
39. Reichstein, M.; Falge, E.; Baldocchi, D.; Papale, D.; Aubinet, M.; Berbigier, P.; Bernhofer, C.; Buchmann, N.; Gilmanov, T.; Granier, A.; et al. On the separation of net ecosystem exchange into assimilation and ecosystem respiration: Review and improved algorithm. *Glob. Change Biol.* **2005**, *11*, 1424–1439. [CrossRef]
40. Friedl, M.A.; Sulla-Menashe, D.; Tan, B.; Schneider, A.; Ramankutty, N.; Sibley, A.; Huang, X. MODIS Collection 5 global land cover: Algorithm refinements and characterization of new datasets. *Remote Sens. Environ.* **2010**, *114*, 168–182. [CrossRef]
41. Stuart, S.N.; Chanson, J.S.; Cox, N.A.; Young, B.E.; Rodrigues, A.S.L.; Fischman, D.L.; Waller, R.W. Status and trends of amphibian declines and extinctions worldwide. *Science* **2004**, *306*, 1783–1786. [CrossRef] [PubMed]
42. IUCN. The IUCN Red List of Threatened Species. Version 2024.2. Available online: http://www.iucnredlist.org (accessed on 14 June 2026).
43. Olson, D.M.; Dinerstein, E.; Wikramanayake, E.D.; Burgess, N.D.; Powell, G.V.N.; Underwood, E.C.; D'Amico, J.A.; Itoua, I.; Strand, H.E.; Morrison, J.C.; et al. Terrestrial Ecoregions of the World: A New Map of Life on Earth. *BioScience* **2001**, *51*, 933–938. [CrossRef]
44. Albert, J.; Rizzo, M. *R Package Stats*; R Foundation for Statistical Computing: Vienna, Austria, 2024.
45. Genuer, R.; Poggi, J.-M.; Tuleau-Malot, C. VSURF: An R package for variable selection using random forests. *R J.* **2015**, *7*, 19–33. [CrossRef]
46. R Core Team. *R: A Language and Environment for Statistical Computing*; R Foundation for Statistical Computing: Vienna, Austria, 2023.
47. Waring, R.H.; Running, S.W. *Forest Ecosystems: Analysis at Multiple Scales*, 2nd ed.; Academic Press: Cambridge, MA, USA, 1999; p. 138.
48. Zhao, Y.; Ma, X.; Zhang, Z.; Liu, K.; Li, W. Leveraging Big Earth Data for spatially explicit tracking of the progress on UN SDG15.1.2 and conservation planning. *Int. J. Digit. Earth* **2025**, *18*, 2506186.
49. Austin, M. Species distribution models and ecological theory: A critical assessment and some possible new approaches. *Ecol. Model.* **2007**, *200*, 1–19. [CrossRef]
50. Jentsch, A.; White, P. A theory of pulse dynamics and disturbance in ecology. *Ecology* **2019**, *100*, e02734. [CrossRef] [PubMed]
51. Bowd, E.; Blanchard, W.; McBurney, L.; Lindenmayer, D. Direct and indirect disturbance impacts on forest biodiversity. *Ecosphere* **2021**, *12*, e03823. [CrossRef]
52. Zhang, F.; Yu, M.; Zhang, J.; He, Y.; Ding, G. Which contributes more in predictor of desert shrubs traits: Intra-annual or inter-annual precipitation change? *Ecol. Indic.* **2024**, *163*, 112037.
53. Wulder, M.A.; Roy, D.P.; Radeloff, V.C.; Loveland, T.R.; Anderson, M.C.; Johnson, D.M.; Healey, S.; Zhu, Z.; Scambos, T.A.; Pahlevan, N.; et al. Fifty years of Landsat science and impacts. *Remote Sens. Environ.* **2022**, *280*, 113195. [CrossRef]
54. Zscheischler, J.; Mahecha, M.D.; Von Buttlar, J.; Harmeling, S.; Jung, M.; Rammig, A.; Randerson, J.T.; Schölkopf, B.; Seneviratne, S.I.; Tomelleri, E.; et al. A few extreme events dominate global interannual variability in gross primary production. *Environ. Res. Lett.* **2014**, *9*, 035001. [CrossRef]
55. Stephenson, P.J.; Stengel, C. An inventory of biodiversity data sources for conservation monitoring. *PLoS ONE* **2020**, *15*, e0242923. [CrossRef] [PubMed]
56. Anderson, R.P.; Araújo, M.B.; Guisan, A.; Lobo, J.M.; Martínez-Meyer, E.; Peterson, A.T.; Soberón, J.M. Optimizing biodiversity informatics to improve information flow, data quality, and utility for science and society. *Front. Biogeogr.* **2020**, *12*, e47787. [CrossRef]
57. Zhang, C.; Cai, D.; Guo, S.; Guan, Y.; Fraedrich, K.; Nie, Y.; Bian, X. Spatial-temporal dynamics of China's terrestrial biodiversity: A dynamic habitat index diagnostic. *Remote Sens.* **2016**, *8*, 227.
58. Razenkova, E.; Radeloff, V.C.; Dubinin, M.; Bragina, E.V.; Allen, A.M.; Clayton, M.K.; Hobi, M.L. Vegetation productivity summarized by the Dynamic Habitat Indices explains broad-scale patterns of moose abundance across Russia. *Sci. Rep.* **2020**, *10*, 836. [CrossRef] [PubMed]
59. Ficetola, G.F.; Rondinini, C.; Bonardi, A.; Katariya, V.; Padoa-Schioppa, E.; Angulo, A. An evaluation of the robustness of global amphibian range maps. *J. Biogeogr.* **2014**, *41*, 211–221.
60. Beck, J.; Böller, M.; Erhardt, A.; Schwanghart, W. Spatial bias in the GBIF database and its effect on modeling species' geographic distributions. *Ecol. Inform.* **2014**, *19*, 10–15. [CrossRef]
61. Zizka, A.; Carvalho, F.A.; Calvente, A.; Baez-Lizarazo, M.R.; Cabral, A.; Coelho, J.F.R.; Antonelli, A. No one-size-fits-all solution to clean GBIF. *PeerJ* **2020**, *8*, e9916. [PubMed]

62. Gaston, K.J. Global patterns in biodiversity. *Nature* **2000**, *405*, 220–227. [CrossRef] [PubMed]
63. Hawkins, B.A.; Field, R.; Cornell, H.V.; Currie, D.J.; Guégan, J.-F.; Kaufman, D.M.; Kerr, J.T.; Mittelbach, G.G.; Oberdorff, T.; O'Brien, E.M.; et al. Energy, water, and broad-scale geographic patterns of species richness. *Ecology* **2003**, *84*, 3105–3117. [CrossRef]
64. Hurlbert, A.H.; Jetz, W. Species richness, hotspots, and the scale dependence of range maps in ecology and conservation. *Proc. Natl. Acad. Sci. USA* **2007**, *104*, 13384–13389. [CrossRef] [PubMed]
65. Radeloff, V.C.; Roy, D.P.; Wulder, M.A.; Anderson, M.; Cook, B.; Crawford, C.J.; Friedl, M.; Gao, F.; Gorelick, N.; Hansen, M.; et al. Need and vision for global medium-resolution Landsat and Sentinel-2 data products. *Remote Sens. Environ.* **2024**, *300*, 113918.
66. Roy, D.P.; Wulder, M.A.; Woodcock, C. Independent oversight crucial to Landsat Next. *Science* **2025**, *388*, 1033. [CrossRef] [PubMed]
67. Sabater, S.; Freixa, A.; Jiménez, L.; López-Doval, J.; Pace, G.; Pascoal, C.; Perujo, N.; Craven, D.; González-Trujillo, J.D. Extreme weather events threaten biodiversity and functions of river ecosystems: Evidence from a meta-analysis. *Biol. Rev.* **2022**, *98*, 450–461. [PubMed]
68. Mahecha, M.D.; Bastos, A.; Bohn, F.J.; Eisenhauer, N.; Feilhauer, H.; Hickler, T.; Quaas, J. Biodiversity and climate extremes: Known interactions and research gaps. *Earth's Future* **2024**, *12*, e2023EF003963. [CrossRef]
69. Clark, J.S.; Iverson, L.; Woodall, C.W.; Allen, C.D.; Bell, D.M.; Bragg, D.C.; D'Amato, A.W.; Davis, F.W.; Hersh, M.H.; Ibanez, I.; et al. The impacts of increasing drought on forest dynamics, structure, and biodiversity in the United States. *Glob. Change Biol.* **2016**, *22*, 2329–2352. [CrossRef] [PubMed]
70. Bastos, A.; Ciais, P.; Friedlingstein, P.; Sitch, S.; Pongratz, J.; Fan, L.; Zaehle, S. Direct and seasonal legacy effects of the 2018 heat wave and drought on European ecosystem productivity. *Sci. Adv.* **2020**, *6*, eaba2724. [CrossRef] [PubMed]
71. Seneviratne, S.I.; Zhang, X.; Adnan, M.; Badi, W.; Dereczynski, C.; Luca, A.D.; Allan, R. Weather and climate extreme events in a changing climate. In *Climate change 2021: The Physical Science Basis: Working Group I Contribution to the Sixth Assessment Report of the Intergovernmental Panel on Climate Change*; Cambridge University Press: Cambridge, UK, 2021; pp. 1513–1766.
72. González-Trujillo, J.D.; Román-Cuesta, R.M.; Muñiz-Castillo, A.I.; Amaral, C.H.; Araújo, M.B. Multiple dimensions of extreme weather events and their impacts on biodiversity. *Clim. Change* **2023**, *176*, 155. [CrossRef]
73. Baldocchi, D.; Chu, H.; Reichstein, M. Inter-annual variability of net and gross ecosystem carbon fluxes: A review. *Agric. For. Meteorol.* **2018**, *249*, 520–533. [CrossRef]
74. Lin, S.; Hu, Z.; Wang, Y.; Chen, X.; He, B.; Song, Z.; Sun, S.; Wu, C.; Zheng, Y.; Xia, X.; et al. Underestimated interannual variability of terrestrial vegetation production by terrestrial ecosystem models. *Glob. Biogeochem. Cycles* **2023**, *37*, e2023GB007696. [CrossRef]
75. De, R.; Brenning, A.; Reichstein, M.; Šigut, L.; Reverter, B.R.; Korkiakoski, M.; Carvalhais, N. Inter–annual variability of model sparameters improves simulation of annual gross primary production. *J. Adv. Model. Earth Syst.* **2026**, *18*, e2025MS005116.
76. Beringer, J.; Hutley, L. FLUXNET2015 AU-How Howard Springs. *FLUXNET2015* 2016. Available online: https://doi.org/10.18140/FLX/1440125 (accessed on 14 June 2026). [CrossRef]
77. Woodgate, W.; van Gorsel, E.; Leuning, R.; Kitchen, M.; Hughes, D.; Zegelin, S. FLUXNET2015 AU-Tum Tumbarumba. *FLUXNET2015* 2016. Available online: https://doi.org/10.18140/FLX/1440126 (accessed on 14 June 2026). [CrossRef]
78. Janssens, I.; Ceulemans, R.; Carrara, A.; Kowalski, A.; Verbeeck, H.; Roland, M.; Neirynck, J.; Gielen, B. FLUXNET2015 BE-Bra Brasschaat. *FLUXNET2015* 2016. Available online: https://doi.org/10.18140/FLX/1440128 (accessed on 14 June 2026). [CrossRef]
79. Ligne, A.; Manise, T.; Moureaux, C.; Aubinet, M.; Heinesch, B. FLUXNET2015 BE-Lon Lonzee. *FLUXNET2015* 2016. Available online: https://doi.org/10.18140/FLX/1440129 (accessed on 14 June 2026). [CrossRef]
80. Ligne, A.; Manise, T.; Heinesch, B.; Aubinet, M.; Vincke, C. FLUXNET2015 BE-Vie Vielsalm. *FLUXNET2015* 2016. Available online: https://doi.org/10.18140/FLX/1440130 (accessed on 14 June 2026). [CrossRef]
81. Restrepo-Coupe, N.; Saleska, S. FLUXNET2015 BR-Sa1 Santarem-Km67-Primary Forest. *FLUXNET2015* 2016. Available online: https://doi.org/10.18140/FLX/1440032 (accessed on 14 June 2026). [CrossRef]
82. Arain, M.A. FLUXNET2015 CA-TP4 Ontario—Turkey Point 1939 Plantation White Pine. *FLUXNET2015* 2016. Available online: https://doi.org/10.18140/FLX/1440053 (accessed on 14 June 2026). [CrossRef]
83. Hörtnagl, L.; Feigenwinter, I.; Fuchs, K.; Merbold, L.; Buchmann, N.; Eugster, W.; Zeeman, M.; Baur, T.; Pluess, P.; Käslin, F.; et al. FLUXNET2015 CH-Cha Chamau. *FLUXNET2015* 2016. Available online: https://doi.org/10.18140/FLX/1440131 (accessed on 14 June 2026). [CrossRef]
84. Hörtnagl, L.; Feigenwinter, I.; Fuchs, K.; Merbold, L.; Buchmann, N.; Eugster, W.; Zeeman, M.; Baur, T.; Pluess, P.; Käslin, F.; et al. FLUXNET2015 CH-Fru Früebüel. *FLUXNET2015* 2016. Available online: https://doi.org/10.18140/FLX/1440133 (accessed on 14 June 2026). [CrossRef]
85. Hörtnagl, L.; Eugster, W.; Buchmann, N.; Paul-Limoges, E.; Etzold, S.; Haeni, M.; Pluess, P.; Baur, T. FLUXNET2015 CH-Lae Laegern. *FLUXNET2015* 2016. Available online: https://doi.org/10.18140/FLX/1440134 (accessed on 14 June 2026). [CrossRef]
86. Hörtnagl, L.; Maier, R.; Eugster, W.; Buchmann, N.; Emmel, C.; Baur, T.; Pluess, P.; Käslin, F.; Meier, P.; Koller, P. FLUXNET2015 CH-Oe2 Oensingen crop. *FLUXNET2015* 2016. Available online: https://doi.org/10.18140/FLX/1440136 (accessed on 14 June 2026). [CrossRef]

87. Sigut, L.; Havrankova, K.; Jocher, G.; Pavelka, M.; Janouš, D.; Stanik, K.; Trusina, J.; Czerny, R. FLUXNET2015 CZ-BK1 Bily Kriz forest. *FLUXNET2015* 2016. Available online: https://doi.org/10.18140/FLX/1440143 (accessed on 14 June 2026). [CrossRef]
88. Brümmer, C.; Lucas-Moffat, A.; Herbst, M.; Kolle, O.; Delorme, J.-P. FLUXNET2015 DE-Geb Gebesee. *FLUXNET2015* 2016. Available online: https://doi.org/10.18140/FLX/1440146 (accessed on 14 June 2026). [CrossRef]
89. Bernhofer, C.; Grünwald, T.; Moderow, U.; Hehn, M.; Eichelmann, U.; Prasse, H.; Postel, U. FLUXNET2015 DE-Gri Grillenburg. *FLUXNET2015* 2016. Available online: https://doi.org/10.18140/FLX/1440147 (accessed on 14 June 2026). [CrossRef]
90. Knohl, A.; Tiedemann, F.; Kolle, O.; Schulze, E.-D.; Kutsch, W.; Herbst, M.; Siebicke, L. FLUXNET2015 DE-Hai Hainich. *FLUXNET2015* 2016. Available online: https://doi.org/10.18140/FLX/1440148 (accessed on 14 June 2026). [CrossRef]
91. Bernhofer, C.; Grünwald, T.; Moderow, U.; Hehn, M.; Eichelmann, U.; Prasse, H.; Postel, U. FLUXNET2015 DE-Kli Klingenberg. *FLUXNET2015* 2016. Available online: https://doi.org/10.18140/FLX/1440149 (accessed on 14 June 2026). [CrossRef]
92. Knohl, A.; Tiedemann, F.; Kolle, O.; Schulze, E.-D.; Anthoni, P.; Kutsch, W.; Herbst, M.; Siebicke, L. FLUXNET2015 DE-Lnf Leinefelde. *FLUXNET2015* 2016. Available online: https://doi.org/10.18140/FLX/1440150 (accessed on 14 June 2026). [CrossRef]
93. Bernhofer, C.; Grünwald, T.; Moderow, U.; Hehn, M.; Eichelmann, U.; Prasse, H.; Postel, U. FLUXNET2015 DE-Tha Tharandt. *FLUXNET2015* 2016. Available online: https://doi.org/10.18140/FLX/1440152 (accessed on 14 June 2026). [CrossRef]
94. Ibrom, A.; Pilegaard, K. FLUXNET2015 DK-Sor Soroe. *FLUXNET2015* 2016. Available online: https://doi.org/10.18140/FLX/1440155 (accessed on 14 June 2026). [CrossRef]
95. Cañete, E.; Ortiz, P.; Jiménez, M.; Poveda, F.; Priego, O.; Ballesteros, A.; Kowalski, A. FLUXNET2015 ES-LJu Llano de los Juanes. *FLUXNET2015* 2016. Available online: https://doi.org/10.18140/FLX/1440157 (accessed on 14 June 2026). [CrossRef]
96. Ourcival, J.-M.; Piquemal, K.; Joffre, R.; Limousin, J.-M. FLUXNET2015 FR-Pue Puechabon. *FLUXNET2015* 2016. Available online: https://doi.org/10.18140/FLX/1440164 (accessed on 14 June 2026). [CrossRef]
97. Bonal, D.; Burban, B. FLUXNET2015 GF-Guy Guyaflux (French Guiana). *FLUXNET2015* 2016. Available online: https://doi.org/10.18140/FLX/1440165 (accessed on 14 June 2026). [CrossRef]
98. Magliulo, V.; Tommasi, P.; Famulari, D.; Gasbarra, D.; Vitale, L.; Manco, A.; Esposito, A.; Tosca, M.; di Matteo, F. FLUXNET2015 IT-BCi Borgo Cioffi. *FLUXNET2015* 2016. Available online: https://doi.org/10.18140/FLX/1440166 (accessed on 14 June 2026). [CrossRef]
99. Matteucci, G. FLUXNET2015 IT-Col Collelongo. *FLUXNET2015* 2016. Available online: https://doi.org/10.18140/FLX/1440167 (accessed on 14 June 2026). [CrossRef]
100. Gianelle, D.; Zampedri, R.; Cavagna, M.; Sottocornola, M. FLUXNET2015 IT-Lav Lavarone. *FLUXNET2015* 2016. Available online: https://doi.org/10.18140/FLX/1440169 (accessed on 14 June 2026). [CrossRef]
101. Gianelle, D.; Cavagna, M.; Zampedri, R.; Marcolla, B. FLUXNET2015 IT-MBo Monte Bondone. *FLUXNET2015* 2016. Available online: https://doi.org/10.18140/FLX/1440170 (accessed on 14 June 2026). [CrossRef]
102. Spano, D.; Duce, P.; Marras, S.; Sirca, C.; Mereu, S.; Arca, A.; Zara, P.; Ventura, A.; Sanna, L. FLUXNET2015 IT-Noe Arca di Noe - Le Prigionette. *FLUXNET2015* 2016. Available online: https://doi.org/10.18140/FLX/1440171 (accessed on 14 June 2026). [CrossRef]
103. Montagnani, L.; Minerbi, S. FLUXNET2015 IT-Ren Renon. *FLUXNET2015* 2016. Available online: https://doi.org/10.18140/FLX/1440173 (accessed on 14 June 2026). [CrossRef]
104. Papale, D.; Arriga, N.; Belelli, L.; Consalvo, C.; Dore, S.; Manca, G.; Mazzenga, F.; Sabbatini, S.; Stefani, P.; Tirone, G.; et al. FLUXNET2015 IT-Ro2 Roccarespampani 2. *FLUXNET2015* 2016. Available online: https://doi.org/10.18140/FLX/1440175 (accessed on 14 June 2026). [CrossRef]
105. Gruening, C.; Goded, I.; Cescatti, A.; Manca, G.; Seufert, G. FLUXNET2015 IT-SRo San Rossore. *FLUXNET2015* 2016. Available online: https://doi.org/10.18140/FLX/1440176 (accessed on 14 June 2026). [CrossRef]
106. Moors, E.; Elbers, J. FLUXNET2015 NL-Loo Loobos. *FLUXNET2015* 2016. Available online: https://doi.org/10.18140/FLX/1440178 (accessed on 14 June 2026). [CrossRef]
107. Biraud, S.; Fischer, M.; Chan, S.; Torn, M. FLUXNET2015 US-ARM ARM Southern Great Plains site-Lamont. *FLUXNET2015* 2016. Available online: https://doi.org/10.18140/FLX/1440066 (accessed on 14 June 2026). [CrossRef]
108. Munger, J.W.; Urbanski, S.; Golden, M.; Barford, C.; Matthes, J.; Wofsy, S. AmeriFlux BASE US-Ha1 Harvard Forest EMS Tower (HFR1), Ver. 27-5. *AmeriFlux AMP* 2026. Available online: https://doi.org/10.17190/AMF/1246059 (accessed on 14 June 2026). [CrossRef]
109. Hanson, C.; Still, C.; Law, B. FLUXNET2015 US-Me2 Metolius mature ponderosa pine. *FLUXNET2015* 2016. Available online: https://doi.org/10.18140/FLX/1440079 (accessed on 14 June 2026). [CrossRef]
110. Novick, K.; Phillips, R. FLUXNET2015 US-MMS Morgan Monroe State Forest. *FLUXNET2015* 2016. Available online: https://doi.org/10.18140/FLX/1440083 (accessed on 14 June 2026). [CrossRef]
111. Suyker, A. FLUXNET2015 US-Ne1 Mead—irrigated continuous maize site. *FLUXNET2015* 2016. Available online: https://doi.org/10.18140/FLX/1440084 (accessed on 14 June 2026). [CrossRef]

112. Suyker, A. FLUXNET2015 US-Ne2 Mead—irrigated maize-soybean rotation site. *FLUXNET2015* 2016. Available online: https://doi.org/10.18140/FLX/1440085 (accessed on 14 June 2026). [CrossRef]
113. Suyker, A. FLUXNET2015 US-Ne3 Mead—rainfed maize-soybean rotation site. *FLUXNET2015* 2016. Available online: https://doi.org/10.18140/FLX/1440086 (accessed on 14 June 2026). [CrossRef]
114. Blanken, P.; Monson, R.; Burns, S.; Bowling, D.; Turnipseed, A.; Knowles, J. FLUXNET2015 US-NR1 Niwot Ridge Forest (LTER NWT1). *FLUXNET2015* 2016. Available online: https://doi.org/10.18140/FLX/1440087 (accessed on 14 June 2026). [CrossRef]
115. Chen, J.; Chu, H.; Noormets, A. FLUXNET2015 US-Oho Oak Openings. *FLUXNET2015* 2016. Available online: https://doi.org/10.18140/FLX/1440088 (accessed on 14 June 2026). [CrossRef]
116. Ma, S.; Xu, L.; Verfaillie, J.; Baldocchi, D. FLUXNET2015 US-Ton Tonzi Ranch. *FLUXNET2015* 2016. Available online: https://doi.org/10.18140/FLX/1440092 (accessed on 14 June 2026). [CrossRef]
117. Ma, S.; Xu, L.; Verfaillie, J.; Baldocchi, D. FLUXNET2015 US-Var Vaira Ranch-Ione. *FLUXNET2015* 2016. Available online: https://doi.org/10.18140/FLX/1440094 (accessed on 14 June 2026). [CrossRef]
118. Kutsch, W.; Merbold, L.; Kolle, O. FLUXNET2015 ZM-Mon Mongu. *FLUXNET2015* 2016. Available online: https://doi.org/10.18140/FLX/1440189 (accessed on 14 June 2026). [CrossRef]

Disclaimer/Publisher's Note: The statements, opinions and data contained in all publications are solely those of the individual author(s) and contributor(s) and not of MDPI and/or the editor(s). MDPI and/or the editor(s) disclaim responsibility for any injury to people or property resulting from any ideas, methods, instructions or products referred to in the content.